

EXPLORING THE ORIGINS OF EARTH'S NITROGEN: ASTRONOMICAL OBSERVATIONS OF NITROGEN-BEARING ORGANICS IN PROTOSTELLAR ENVIRONMENTS

THOMAS S. RICE¹ AND EDWIN A. BERGIN
University of Michigan Department of Astronomy
311 West Hall, 1085 South University Avenue,
Ann Arbor, MI 48109, USA

JES K. JØRGENSEN
Centre for Star and Planet Formation,
Niels Bohr Institute & Natural History Museum of Denmark,
University of Copenhagen,
Øster Voldgade 5-7, 1350, Copenhagen K., Denmark

S. F. WAMPFLER
Center for Space and Habitability, University of Bern, Gesellschaftsstrasse 6, CH-3012 Bern, Switzerland

¹tsrice@umich.edu

ABSTRACT

It is not known whether the original carriers of Earth's nitrogen were molecular ices or refractory dust. To investigate this question, we have used data and results of *Herschel* observations towards two protostellar sources: the high-mass hot core of Orion KL, and the low-mass protostar IRAS 16293–2422. Towards Orion KL, our analysis of the molecular inventory of [Crockett et al. \(2014b\)](#) indicates that HCN is the organic molecule that contains by far the most nitrogen, carrying $74^{+5}_{-9}\%$ of nitrogen-inorganics. Following this evidence, we explore HCN towards IRAS 16293–2422, which we consider a solar analog. Towards IRAS 16293–2422, we have reduced and analyzed *Herschel* spectra of HCN, and fit these observations against “jump” abundance models of IRAS 16293–2422's protostellar envelope. We find an inner-envelope HCN abundance $X_{\text{in}} = 5.9 \pm 0.7 \times 10^{-8}$ and an outer-envelope HCN abundance $X_{\text{out}} = 1.3 \pm 0.1 \times 10^{-9}$. We also find the sublimation temperature of HCN to be $T_{\text{jump}} = 71 \pm 3$ K; this measured T_{jump} enables us to predict an HCN binding energy $E_{\text{B}}/k = 3840 \pm 140$ K. Based on a comparison of the HCN/H₂O ratio in these protostars to N/H₂O ratios in comets, we find that HCN (and, by extension, other organics) in these protostars is incapable of providing the total bulk N/H₂O in comets. We suggest that refractory dust, not molecular ices, was the bulk provider of nitrogen to comets. However, interstellar dust is not known to have ¹⁵N enrichment, while high ¹⁵N enrichment is seen in both nitrogen-bearing ices and in cometary nitrogen. This may indicate that these ¹⁵N-enriched ices were an important contributor to the nitrogen in planetesimals and likely to the Earth.

Keywords: ISM: molecules – stars: protostars – astrochemistry – comets: general – planets and satellites: formation – ISM: abundances – ISM: individual objects (Orion KL, IRAS 16293–2422)

1. INTRODUCTION

Earth's nitrogen is a key element for life as well as the primary component of our atmosphere. Because of the high volatility of the key nitrogen carriers in the interstellar medium (atomic N and N₂), it is expected that the building blocks of terrestrial worlds would be nitrogen-poor; as a consequence, the origin of Earth's nitrogen is uncertain. The most likely origin scenario is impact delivery by asteroids (probed by meteorites) or icy planetesimals (e.g., comets; [Morbidelli et al. 2012](#)). The most recent work suggests an origin in delivery from chondritic meteorites, with a smaller role played by comets ([Marty et al. 2016](#); [Alexander et al. 2017](#), and references therein).

In chondrites (the most primitive meteorites), nitrogen is contained in a macromolecular organic form that is insoluble by both acids and solvents, typically known as insoluble organic matter (IOM). As chondrites are the most primitive and most volatile-rich of the meteorites, chondritic IOM is likely the source of the carbon, nitrogen, noble gases, and much of the hydrogen that were delivered to terrestrial planets (Alexander et al. 2012; Marty 2012; Marty et al. 2013; Alexander et al. 2017). The IOM or its chemical precursors likely formed in the outer solar system and/or the interstellar medium (Charnley & Rodgers 2008), but it is unknown whether the IOM has a primarily solar or pre-solar origin, or a mix (Alexander et al. 2017, and references therein). Bergin et al. (2014); Bergin et al. (2015) have discussed the astronomical origins of terrestrial carbon, arguing that the initial carriers of terrestrial carbon and nitrogen are organic ices and macromolecular organic material, including dust.

Nitrogen is contained in a variety of molecular and physical carriers in interstellar space, each of which has its own properties – including its volatility (i.e., its sublimation temperature) and its ability to undergo isotopic fractionation (i.e., change its $^{14}\text{N}/^{15}\text{N}$ ratio). Little is known about which initial carriers could have brought nitrogen into chondritic IOM, but two aspects are relevant. First, while the most volatile forms of nitrogen (atomic N and molecular N_2) likely contain the vast majority of nitrogen atoms in the dense interstellar medium (e.g., van Dishoeck et al. 1993; Schwarz & Bergin 2014), their volatility prevents them from readily incorporating into solid material, so the IOM’s nitrogen likely came from carriers with lower volatility. Second, the nitrogen of the IOM is known to be highly enriched ^{15}N compared to the ISM standard (Füri & Marty 2015; Alexander et al. 2017). These factors lead us to consider two families of nitrogen carriers: nitrogen-bearing molecular ices, especially organics, and nitrogen contained in interstellar dust solids (i.e., refractory nitrogen).

Refractory nitrogen has not been directly observed. However, depletion in the gas-phase atomic nitrogen abundance in the diffuse ISM has been observationally constrained by Knauth et al. (2003) and Jensen et al. (2007). This is generally interpreted as due to nitrogen incorporation into dust grains. Jones (2016) discusses the role of nitrogen in models of interstellar carbonaceous dust.

Some nitrogen-bearing molecular ices, especially including hydrogen cyanide (HCN), exhibit a high ^{15}N enrichment in interstellar environments (e.g., Hily-Blant et al. 2013; Wampfler et al. 2014; Guzmán et al. 2017) and have a high abundance in the dense ISM (e.g., Crockett et al. 2014b; Zernickel et al. 2012; Schöier et al. 2002, etc.). HCN itself also has a rich chemical reactivity (as noted by, e.g., Noble et al. 2013). Ammonia (NH_3) is another very abundant ice constituent, but in the gas does not seem to show the same isotopic signature (Hily-Blant et al. 2013). Motivated by these factors, we here investigate HCN and the family of organic (C-bearing) molecular carriers of nitrogen in their possible role as the initial reservoir of nitrogen that ultimately arrives on terrestrial worlds.

A powerful way to probe the origins of nitrogen in the solar system is through astronomical observations of other forming planetary systems. The success over the past decade of the *Herschel* Space Observatory in submillimeter and far-infrared astronomy has brought a wealth of data and knowledge to the observational astrochemistry community, enabling new frontiers of molecular astrophysics. In this study, we have drawn upon the data and results from these projects, especially the spectral surveys of Orion KL (Bergin et al. 2010; Crockett et al. 2014b) and IRAS 16293–2422 (Ceccarelli et al. 2010; Coutens et al. 2012). The high-mass hot core of Orion KL exhibits a rich molecular spectrum. It represents an environment in which the molecular ices available to planet-forming materials are revealed via sublimation, and hence can be studied astronomically. The molecular abundance inventory presented by Crockett et al. (2014b) of Orion KL enables an investigation of the relative abundances of many molecular species, especially (for our purposes) nitrogen-bearing organics. The rich HIFI spectrum of IRAS 16293–2422, a solar-type low-mass protostar, is also available in the Herschel Science Archive. This spectrum can extend analyses from ground-based studies (e.g., Schöier et al. 2002; Caux et al. 2011; Wampfler et al. 2014; Jørgensen et al. 2016) and unlock the molecular content of IRAS 16293–2422’s envelope, especially in its warm inner regions.

In this project, our goal is to study the distribution of nitrogen among different organic molecules, and to compare the protostellar abundance of HCN, the simplest nitrogen-bearing organic, to nitrogenic abundances in comets relative to water. In Section 2, we introduce the observations and data used in this work, which consist of *Herschel* observations towards Orion KL and IRAS 16293–2422. In Section 3, we give an accounting of the nitrogen-bearing organic molecules in the Orion KL Hot Core. In Section 4, we report on our analysis of *Herschel* HIFI data towards IRAS 16293–2422, and present our derivation of the HCN radial abundance distribution as inferred from a spherically symmetric model. We discuss our results in Section 5 in the context of cometary nitrogen abundances, and consider the available evidence pertaining to comets, meteorites, interstellar dust, and interstellar ices. We present our conclusions in Section 6.

2. DATA AND OBSERVATIONS

We have analyzed the results of Herschel observations towards the protostellar environments of Orion KL and IRAS 16293–2422 (henceforth IRAS 16293). Each of these Herschel observations made use of the Heterodyne Instrument for the Far-Infrared (HIFI) spectrograph, and included a spectral survey with large (~ 1 THz) bandwidth, fine resolution, and high sensitivity. These observations are part of the HEXOS (Herschel Observations of EXtra-Ordinary Sources; [Bergin et al. 2010](#)) and CHESS (Chemical HErschel Surveys of Star forming regions; [Ceccarelli et al. 2010](#)) large programs. Additional ground-based observations of IRAS 16293 from [Wampfler et al. \(2014\)](#) and from the TIMASSS program ([Caux et al. 2011](#)) complement the HIFI data in our analysis.

Orion KL —

We use observations of Orion KL from the HEXOS program ([Bergin et al. 2010](#)); these observations and their reduction were described in detail in [Crockett et al. \(2014b\)](#). The dataset consists of a ~ 1.2 THz-wide spectrum from 480 to 1907 GHz at a resolution of 1.1 MHz. These data were previously presented and analyzed in [Crockett et al. \(2010\)](#); [Wang et al. \(2011\)](#); [Plume et al. \(2012\)](#); [Neill et al. \(2013a,b\)](#), and [Crockett et al. \(2014a,b, 2015\)](#). In this paper, we primarily analyze the molecular abundances of the Orion KL Hot Core presented in [Crockett et al. \(2014b\)](#) and [Neill et al. \(2013b\)](#); we additionally use results from the 1.3 cm survey of Orion KL by [Gong et al. \(2015\)](#).

IRAS 16293–2422 —

We have freshly reduced and analyzed the HIFI observations of IRAS 16293 from the CHESS program ([Ceccarelli et al. 2010](#)). This spectrum spans 0.9 THz from 480–1800 GHz, with gaps, and again has a spectral resolution of 1.1 MHz. These data were previously presented and analyzed in [Hily-Blant et al. \(2010\)](#); [Bacmann et al. \(2010\)](#), and [Coutens et al. \(2012\)](#). We obtained the *Herschel* HIFI spectra of IRAS 16293 from the Herschel Science Archive (<http://archives.esac.esa.int/hsa/whsa/>) and downloaded the Level 2.5 products. We averaged the horizontal and vertical polarizations in GILDAS/CLASS to improve the signal-to-noise. Finally, we resampled all lines to a common velocity resolution of 0.7 km s^{-1} , the resolution of the lowest- J line, in order to achieve consistency between lines and improve the per-channel signal-to-noise.

We have complemented our HIFI data of IRAS 16293 with two sets of ground-based data covering lower-energy transitions. We have used observations of IRAS 16293 at 260 and 345 GHz from the Atacama Pathfinder EXperiment (APEX) 12-meter telescope in Chile. These APEX data were previously presented in [Wampfler et al. \(2014\)](#), where a detailed description of these data appears. Finally, for the 86 GHz $J = 1 - 0$ transition of H^{13}CN , we have used the publicly available reduced TIMASSS data ([Caux et al. 2011](#)).

3. NITROGEN-BEARING MOLECULES IN THE ORION KL HOT CORE

3.1. Background

[Crockett et al. \(2014b\)](#) analyzed the HEXOS spectra of Orion KL and identified $\sim 13,000$ lines coming from 39 molecules (79 distinct isotopologues). This study made use of IRAM-30m data (80–280 GHz) to constrain low-energy molecular transitions, and of an ALMA interferometric spectral survey at 214–247 GHz to constrain both the millimeter spectrum and the spatial structure of the continuum and molecular emission. Spatial information is especially important due to the multiple physical components within Orion KL which are not spatially resolved by *Herschel*. [Crockett et al.](#) present ALMA maps of various molecules, indicating that, e.g., CH_3CN and CH_3OH , fill the Hot Core’s spatial extent as traced by its continuum emission.

[Crockett et al.](#) modeled the emission from each component individually. Temperature gradients within the Hot Core were approximated using the following approach: A single $10''$ component was fit to the emission of each molecule. If a single-temperature component was not sufficient to reproduce the observed emission, then additional subcomponents were added, either larger and cooler or smaller and hotter, in size steps of factor two. [Crockett et al.](#) use two modeling codes: a local thermodynamic equilibrium (LTE) code called XCLASS, and a non-LTE, large velocity gradient (LVG) code called MADEX ([Cernicharo 2012](#)). These emission modeling codes were used to derive column densities and abundances for all observed species. The water abundances, in particular, were derived by [Neill et al. \(2013b\)](#). Among the physical components of Orion KL, we have focused on the Hot Core as the most relevant astrochemical environment in which ices are evaporating, revealing the total molecular budget available at this stage of star and planet formation; in the other regions, many molecules which are important to planetesimal formation are hidden in ices.

Additional abundances of nitrogen-bearing organics in Orion KL are available in the recent literature. Formamide (NH_2CHO) was measured by [Adande et al. \(2013\)](#) towards Orion KL with an abundance of 5×10^{-11} , but because the Hot Core was not spatially or kinematically resolved in their measurement, we omit formamide from our analysis. [Crockett et al. \(2014b\)](#) identified NH_2CHO emission only towards the compact ridge of Orion KL, and not the Hot Core, further justifying this exclusion. In any case, its abundance appears to be far below that of HCN. Another N-

bearing organic, methyl isocyanate (CH_3NCO), was measured in Orion KL by [Cernicharo et al. \(2016\)](#), who identified abundances towards distinct spatial positions within Orion KL. They measured the CH_3NCO abundance (relative to H_2O) towards a position collocated with the Hot Core. By scaling the fractional abundance of CH_3NCO relative to HCN and CH_3CN found by [Cernicharo et al. \(2016\)](#) to the abundances of HCN and CH_3CN in the Orion KL Hot Core found by [Crockett et al. \(2014b\)](#), we estimate the CH_3NCO abundance relative to H_2 in the Hot Core to be in the range $3 \times 10^{-9} - 1 \times 10^{-8}$.

The cyanide radical (CN) is a common molecule in the cool and relatively less-dense molecular ISM, but is not abundant in the Orion KL Hot Core. CN is destroyed rapidly in hot cores via reactions with H_2 , oxygen (O and O_2), and simple hydrocarbons such as C_2H_2 and C_2H_4 ([Tielens & Charnley 2013](#); [Whittet 2013](#)). Accordingly, CN is not detected by [Crockett et al. \(2014b\)](#) in either the Hot Core or the compact ridge; they find it only towards the plateau and extended ridge regions of Orion KL, where its low rotation temperature of $\sim 20 - 40$ K indicates that CN emission probes cool material.

Ammonia (NH_3) is another nitrogen carrier of interest. [Crockett et al. \(2014b\)](#) were unable to derive an abundance of NH_3 towards Orion KL as the *Herschel* survey did not detect lines spanning a sufficiently large upper-state energy coverage to constrain the abundance and excitation state of the gas. NH_3 was studied observationally towards Orion KL by [Gong et al. \(2015\)](#), who performed a 1.3 cm line survey of the region with the Effelsberg-100 m telescope; their results are noted below alongside those of [Crockett et al. \(2014b\)](#).

3.2. Analysis

In order to study the composition of nitrogen-bearing organic (C-containing) molecules, we have analyzed the molecular abundances presented by [Crockett et al. \(2014b\)](#). To do this, we isolated the abundances ($N(X)/N_{\text{H}_2}$, where N represents a column density in cm^{-2}) of all compounds containing both carbon and nitrogen from Table 8 of [Crockett et al. \(2014b\)](#). We calculate the total amount of organic nitrogen by adding all N atoms contained in organic molecules¹. Each molecule’s fraction of organic nitrogen corresponds to the number of N atoms contained in that molecule, divided by the sum of N in organics. [Crockett et al. \(2014b\)](#) estimate that individual column density measurements have an uncertainty of 25%. We estimate uncertainties on the relative abundances to be 35%, by taking each molecule’s column density uncertainty to be independent and adding their uncertainties in quadrature. For CH_3NCO , we assign an additional $\sim 50\%$ uncertainty on the higher and lower ends of the abundance range scaled from the measurements in [Cernicharo et al. \(2016\)](#), by adding in quadrature the relative errors on column densities in their measurements to those in [Crockett et al. \(2014b\)](#); this accounts for the differences in observing setups. We show the distribution of N atoms among organic species in Figure 1, on a logarithmic percentage scale with appropriate error bars (left) and in a linear pie-chart form (right).

3.3. Results

The total abundance (relative to H_2) of N atoms in organic (C-containing) molecules in Orion KL Hot Core is $8.6 \pm 3.4 \times 10^{-7}$. HCN, with an abundance of $X(\text{HCN}) = 6.4 \pm 2.5 \times 10^{-7}$, is the most abundant N-bearing organic, containing $74_{-9}^{+5}\%$ of all N atoms that are in organic molecules. The next most abundant species are $\text{C}_2\text{H}_5\text{CN}$ (ethyl cyanide), with abundance $8.9 \pm 3.5 \times 10^{-8}$, containing $10 \pm 3\%$ of N atoms within organic molecules; HNCO (isocyanic acid), with abundance $7.8 \pm 3.1 \times 10^{-8}$, containing $9 \pm 3\%$ of organic N atoms; and CH_3CN (methyl cyanide), with abundance $3.0 \pm 1.2 \times 10^{-8}$, containing $3 \pm 1\%$ of organic N atoms. The remaining observed species ($\text{C}_2\text{H}_3\text{CN}$, HC_3N , CH_3NCO , CH_2NH , and HNC) each constitute $\lesssim 1\%$ of the nitrogen budget among organic molecules. Therefore, HCN accounts for more than two-thirds of the organic N budget.

Some abundant N-bearing non-organic species are excluded from the above analysis but have known abundances. As noted above, NH_3 was observed by [Gong et al. \(2015\)](#). Their measurements of many NH_3 , $^{15}\text{NH}_3$, and NH_2D lines suggest an NH_3 abundance in the range $0.8 - 6 \times 10^{-6}$. This range indicates that the NH_3 abundance is at least equal to, and possibly an order of magnitude higher than, the abundance of HCN in the Orion KL Hot Core. The NO abundance derived by [Crockett et al. \(2014b\)](#) is 5.5×10^{-7} , which is consistent (within the errors) with the HCN abundance. Also, [Crockett et al. \(2014b\)](#) derive an NS abundance of 6.8×10^{-9} .

3.4. Limitations, caveats, and comments of hot core analysis

¹ In principle, molecules with multiple nitrogen atoms would count multiply to this total, in proportion to the number of N atoms they possessed; however, all N-bearing organics in this table have just one N atom, so this sum is identical to the amount of N-bearing organic molecules.

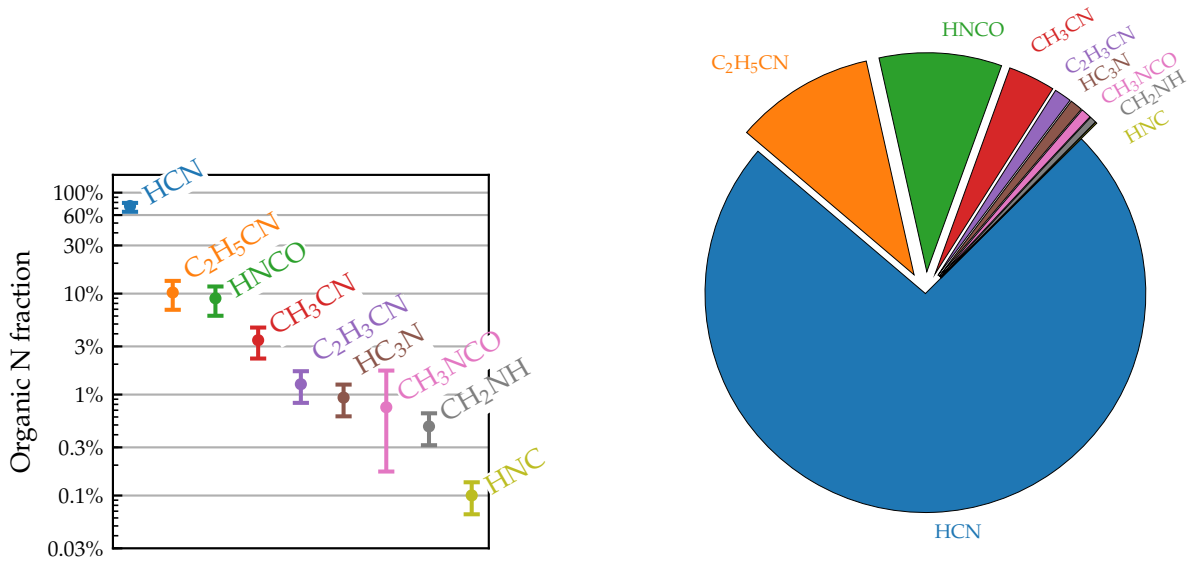


Figure 1. Accounting of organic nitrogen-bearing molecules in Orion KL Hot Core, from abundances presented in Crockett et al. (2014b) and (for CH₃NCO) Cernicharo et al. (2016). Left: Fraction of total nitrogen found in organic species, per molecule. Right: Pie chart of the mean fraction for each species. The larger errors for CH₃NCO are described in the text.

The abundance measurements of Crockett et al. (2014b) depend on the accuracy of the H₂ column density measured in Plume et al. (2012), which was itself scaled from an empirical measurement of C¹⁸O column density using an H₂:C¹⁸O ratio of 5×10^6 ; therefore, any issues in CO:H₂ scaling would complicate the abundance measurements. The molecular column densities derived for the Orion KL Hot Core observed by *Herschel*, as presented in Crockett et al. (2014b), depend on assumed source sizes. For Orion KL, Crockett et al. (2014b) and Plume et al. (2012) assume the same source size for the Hot Core, so any errors should cancel out.

One issue that may complicate the interpretation of the *Herschel* molecular abundance inventories is the following ambiguity. As noted in Crockett et al. (2015), there are two ways to account for the increased abundances of many molecules in the Orion KL Hot Core:

1. Grain surface chemistry at cold temperatures that produces icy molecules which are then sublimated (and thus revealed) by the high-temperature environment of the hot core; or
2. Hot gas chemistry that produces gas molecules in-situ, which only operates in the hot environment.

Our interpretation assumes that the observed molecular populations are dominated by molecules which are formed under the cold conditions of option (1) and are simply *revealed* by the hot environment, as opposed to molecules which *form* due to the hot environment. Crockett et al. (2015) suggested two ways to probe this further. First, to look for spatial gradients in the D/H ratios of complex N-bearing species, as this would be a sign of grain surface chemistry. Second: in the scenario in which the N-bearing organics are desorbing at higher temperatures than O-bearing organics, rather than forming in the hot gas itself, we would expect to see that the emission from N-bearing species is clumpier and has a higher excitation temperature on average.

Among nitrogen-bearing organics, Crockett et al. (2014b) modeled CH₃CN, HCN, and HNC with both the XCLASS (simple LTE) and MADEX (non-LTE, large velocity gradient) molecular line spectra modeling codes. The abundances derived for CH₃CN are identical using both methods; compared to XCLASS, the HCN abundance from MADEX is a factor $1.7\times$ higher; and the HNC abundance from MADEX is a factor $6.3\times$ lower. The MADEX modeling is thought to yield more accurate abundances, as it is more sophisticated and can account for both temperature and density gradients, so we preferentially show MADEX results where possible. We note that our results do not change substantially when only XCLASS abundances are used.

Regardless of the above caveats and limitations on the absolute abundance measurements, our results clearly indicate that in a relative comparison, HCN is the dominant N-bearing organic molecule in the Orion KL Hot Core.

While our analysis of Orion KL is valuable especially due to its rich available spectrum, Orion KL has a higher mass than the region in which the Sun formed, and there may be chemical differences between a high-mass hot core and the birth environment of our Sun. To attempt to control for this difference, we have also studied the low-mass protostar IRAS 16293. IRAS 16293 is a low-mass protostar benchmark, and is among the brightest low-mass protostellar sources in molecular line emission (see [Jørgensen et al. 2016](#) for an extended review of the literature on this source). Motivated by the high abundance of HCN among organic N-bearing molecules towards Orion KL, we have measured the HCN content towards IRAS 16293. In this measurement, we have made use of the ground-based measurements of low- J states presented in [Caux et al. \(2011\)](#) and [Wampfler et al. \(2014\)](#), and space-based high- J states from *Herschel* ([Ceccarelli et al. 2010](#)). We have fit a spherically symmetric “jump abundance” model to the observed HCN lines, in order to derive the HCN abundance within and outside the warm sublimation zone.

4.1. Background

IRAS 16293 is a prototypical Class 0 protostellar system which has been well-characterized physically and chemically. It lies at a distance of ~ 120 pc ([Loinard et al. 2008](#)) and has a luminosity of $21 \pm 5 L_{\odot}$ ([Jørgensen et al. 2016](#)). It is a protobinary, with two major components (*IRAS16293A* and *IRAS16293B*) that have a separation of $5.1''$ or ~ 620 AU ([Looney et al. 2000](#); [Jørgensen et al. 2016](#)). IRAS16293A is itself a possible tight binary with separation $1''$ ([Chandler et al. 2005](#)). IRAS 16293 is notable for its rich molecular line spectrum ([van Dishoeck et al. 1995](#); [Cazaux et al. 2003](#)) and has been the target of numerous single-dish and interferometric studies, most recently the ALMA-PILS survey ([Jørgensen et al. 2016](#); [Lykke et al. 2017](#); [Ligterink et al. 2017](#)). Combined interferometric and single-dish imaging of HCN and HC^{15}N lines was presented by [Takakuwa et al. \(2007\)](#). Within this system, an inner “hot corino” of $\gtrsim 100$ K gas enriched with evaporated ices is thought to be present, in order to explain molecular abundance jumps and rich organic chemistry ([Schöier et al. 2002](#); [Cazaux et al. 2003](#)). Consequently, it is an excellent low-mass protostellar astrochemical benchmark, especially for our interest in studying icy nitrogen materials provided to early planetesimals.

The nitrogen-bearing organics in the hot corino of IRAS 16293 are not as well-constrained as those in Orion KL, so it is difficult to quantify whether nitrogen has major chemical differences in IRAS 16293 versus Orion KL. Nonetheless, unpublished and recently-published results on column densities of nitriles ($-\text{C}\equiv\text{N}$ -bearing organics) are consistent with HCN containing the majority of N in organics in IRAS 16293. Using the PILS data, [Calcutt et al. \(2018a,b\)](#) studied complex nitriles in IRAS 16293 including CH_3CN , $\text{C}_2\text{H}_5\text{CN}$, $\text{C}_2\text{H}_3\text{CN}$, HC_3N , and CH_3NC . Of these, CH_3CN is by far the most abundant; it is an order of magnitude more abundant than the next most abundant species, $\text{C}_2\text{H}_5\text{CN}$. PILS measurements of HCN and its isotopologues are still unpublished; an analysis of the optically-thick (on $0''.5$ scales) HC^{15}N 4–3 line at 344.2 GHz indicates that HC^{15}N is at least $1.6\times$ as abundant as $\text{CH}_3\text{C}^{15}\text{N}$, and therefore (assuming that ^{15}N fractionation is comparable between HCN and CH_3CN) that HCN is at least $1.6\times$ as abundant as CH_3CN , and therefore the dominant organic N carrier in IRAS 16293.

4.2. Herschel Data Reduction

We fit lines of HCN, H^{13}CN and HC^{15}N from $J = 6 - 5$ to $10 - 9$ with Gaussian profiles². Because some of the H^{13}CN and HC^{15}N lines are quite weak, we have used the line widths and velocity centers of the corresponding HCN lines for either (a) an initial guess for the Gaussian fit, or (b) a fixed parameter such that only the line intensity was allowed to float in the fit, depending on the strength of the lower-intensity line. Results of this fitting are presented in Appendix A; Figure A1 shows the lines and their Gaussian fits, and the fitted line parameters are presented in Table A1.

We have estimated the optical depths from the flux ratios between the standard isotopologue HCN and its rarer isotopologue H^{13}CN . By assuming an isotopic ratio between HCN and H^{13}CN , we can relate the optical depth of a given rarer isotopologue in the following way (as described by [Crockett et al. 2014a](#)):

$$\tau_{\text{iso}} = -\ln\left(1 - \frac{T_{\text{iso}}}{T_{\text{main}}}\right) \quad (1)$$

and

$$\tau_{\text{main}} = \tau_{\text{iso}} \cdot \left(\frac{^{12}\text{C}}{^{13}\text{C}}\right). \quad (2)$$

² We note that the HC^{15}N 7–6 line is blended with a stronger adjacent SO $J = 14 - 13$ line at 602.292 GHz; we fit the two lines simultaneously.

Table 1. Lines of H¹³CN used to fit model.

Line	E_{up} (K)	Freq (GHz)	Telescope	Pointing offset ^a (")	Beamsize HPBW (")
1 – 0	4.1	86.340	IRAM	5.0	29.1
3 – 2	24.9	259.012	APEX	0.0	24.3
4 – 3	41.4	345.340	APEX	0.0	18.2
6 – 5	87.0	517.970	HIFI	2.5	41.6
7 – 6	116.0	604.268	HIFI	2.5	35.7
8 – 7	149.2	690.552	HIFI	2.5	31.2
9 – 8	186.4	776.820	HIFI	2.5	27.7
10 – 9	227.9	863.071	HIFI	2.5	25.0
11 – 10	273.4	949.301	HIFI	2.5	22.7

^aPointing offsets from source A are described in [Caux et al. \(2011\)](#) for the IRAM data, [Wampfler et al. \(2014\)](#) for the APEX data, and [Coutens et al. \(2012\)](#) for the HIFI data.

NOTE—Gaussian fits to these lines, and their HCN and HC¹⁵N counterparts, appear in [Table A1](#) in [Appendix A](#).

In these equations, T_{main} and T_{iso} denote the peak brightness temperatures of the main and rarer isotopologue lines, respectively, and τ_{main} and τ_{iso} likewise denote those lines’ optical depths. This equation assumes that $\tau_{\text{main}} \gg \tau_{\text{iso}}$, which is appropriate for comparing ¹²C with ¹³C. We adopt a carbon isotopic ratio of $^{12}\text{C}/^{13}\text{C} = 69 \pm 6$ in the local ISM ([Wilson 1999](#)). The optical depths τ are given in [Table A2](#). We found optical depths $\tau_{\text{H}^{13}\text{CN}} = 0.08 - 0.24$ (corresponding to $\tau_{\text{HCN}} = 5.9 - 16.5$). Therefore, we can confirm that none of the H¹³CN lines is optically thick.

4.3. Nitrogen Isotopic Fractionation

Nitrogen isotopic fractionation seen in a low-mass protostellar system such as IRAS 16293 can be compared to the nitrogen fractionation measured in solar system objects such as meteorites and comets ([Hily-Blant et al. 2013](#); [Füri & Marty 2015](#)). By assuming that H¹³CN and HC¹⁵N have the same excitation properties in IRAS 16293, and with knowledge (from the HCN lines) that the observed H¹³CN and HC¹⁵N lines are all optically thin ($\tau \lesssim 0.25$), we can calculate the ¹⁴N/¹⁵N ratio for each rotational state of HCN independently. In the *Herschel* data, the following lines have definite detections for both H¹³CN and HC¹⁵N: 6 – 5, 7 – 6, 8 – 7, and 9 – 8. We find the ¹⁴N/¹⁵N ratio in each line to be 119 ± 13 , 155 ± 43 , 151 ± 89 , and 210 ± 70 respectively. In all cases, these are ¹⁵N-enriched relative to the local ISM ¹⁴N/¹⁵N ratio of 388 ± 38 and the solar standard of 270 ([Wilson 1999](#)). These results are broadly consistent with the ¹⁴N/¹⁵N ratios measured by [Wampfler et al. \(2014\)](#) for this source, in which the 4 – 3 and 3 – 2 lines had 190 ± 38 and 163 ± 20 , respectively. The weighted mean of the ¹⁴N/¹⁵N values is 140 ± 10 .

4.4. Model

In order to derive the HCN abundance profile around IRAS 16293, we have used spherically symmetric models of the temperature, density, and molecular abundance in order to produce model spectra and compare them with the observed emission from H¹³CN. We focus on this isotopologue, which has a much lower abundance than HCN and therefore fewer issues with optical depth. Aspects of this model fitting are similar to the approach carried out by [Coutens et al. \(2012\)](#), who use the physical model of IRAS 16293 derived in [Crimier et al. \(2010\)](#). We choose this modeling approach to derive the HCN abundance in a way that is consistent with the previous H₂O abundance modeling performed by [Coutens et al. \(2012\)](#). This facilitates direct comparison of these results and yield HCN/H₂O ratios, though as noted by [Visser et al. 2013](#) and further discussed in [Section 5.1](#), the [Coutens et al.](#) water abundance of 5×10^{-6} is possibly only a lower limit, with theoretical and observational support for a value closer to 10^{-4} .

We use a model which has two regions of constant HCN abundance: an outer “cold” region with a low gas-phase HCN abundance (because most HCN is frozen onto dust grains), and an inner “warm” region with a high gas-phase HCN abundance due to sublimation of HCN from those grains. This “jump abundance” model has three free parameters: The inner abundance (X_{in}), the outer abundance (X_{out}), and the temperature at which sublimation rapidly occurs

Table 2. Parameters for H¹³CN emission model of IRAS 16293–2422

Fixed parameters		
L_* (L_\odot)	22	
D (pc)	120	
r_{\min} (AU)	22	
r_{\max} (AU)	6100	
r_{infall} (AU)	1280	
ρ power law index	-1.5	($r < r_{\text{infall}}$)
	-2	($r > r_{\text{infall}}$)
M_{env} (M_\odot)	1.9	
M_* (M_\odot)	1.0	

Floating parameters		
	Best-fit (\pm)	Allowed Range
X_{in} (H ¹³ CN)	$8.51^{+0.81}_{-0.74} \times 10^{-10}$	$10^{-12} - 10^{-8}$
X_{out} (H ¹³ CN)	$1.82^{+0.09}_{-0.09} \times 10^{-11}$	$10^{-14} - X_{\text{in}}$
T_{jump} (K)	$71.2^{+2.4}_{-2.6}$	30 – 120

MCMC parameters	
# walkers	24
# steps	1776
Autocorrelation time τ	34.7
# steps / τ	51.2

NOTE—We adopt fixed physical parameters for our IRAS 16293 model following [Crimier et al. \(2010\)](#) and [Coutens et al. \(2012\)](#).

(T_{jump}). Jump abundance models have been adopted to interpret observations of protostars in many papers (e.g., [Schöier et al. 2002](#); [Maret et al. 2004](#); [Parise et al. 2005](#); [Brinch et al. 2009](#); [Coutens et al. 2012](#)). The sublimation rate of molecular ices depends exponentially on the local temperature, so a step-function is an appropriate way to model the very steep increase that occurs in gas-phase molecular abundances at specific radii ([Rodgers & Charnley 2003](#); [Jørgensen et al. 2005](#)).

We present the parameters used in this model in Table 2. To enable direct comparison with [Coutens et al. \(2012\)](#), who derived the H₂O abundance using a very similar set of data and methods, we adopt the one-dimensional physical model developed by [Crimier et al. \(2010\)](#). This physical model incorporates (a) submillimeter single-dish emission profiles at 350, 450, and 850 μm , and (b) the spectral energy distribution (SED) from 23 to 1300 μm . [Crimier et al. \(2010\)](#) present a model of the density and temperature structure which follows a Shu “inside-out” collapsing envelope ([Shu 1977](#); [Adams & Shu 1986](#)), in which the density follows two power laws: $\rho \propto r^{-1.5}$ for $r < r_{\text{infall}}$, and $\rho \propto r^{-2}$ for $r > r_{\text{infall}}$. Three-dimensional models of the physical structure of IRAS 16293 are under development (e.g., [Jacobsen et al. 2017](#), who model the envelope, disks and dust filament), but for the purposes of this paper, a 1D model is sufficient to derive bulk abundance properties.

In our modeling, we start with the luminosity and density distributions listed in Table 2, and first solve for the temperature structure using the radiative transfer code TRANSPHERE ([Dullemond et al. 2002](#))³. Following [Coutens et al. \(2012\)](#), we use RATRAN ([Hogerheijde & van der Tak 2000b,a](#); [van der Tak & Hogerheijde 2007](#)), a spherical Monte Carlo 1D radiative transfer code: RATRAN solves the line radiative problem by iteratively computing the mean

³ The TRANSPHERE Fortran code is hosted online at <http://www.ita.uni-heidelberg.de/~dullemond/software/transphere/index.shtml>

radiation field J_ν in each radial shell to derive the level populations of H^{13}CN . The HCN collision rate coefficients were derived by [Dumouchel et al. \(2010\)](#) with He as the collision partner. The rates were retrieved in a molecular data file from the LAMDA database⁴ ([Schöier et al. 2005](#)), where they were scaled by a factor 1.37 to represent collisions with H_2 . Like [Coutens et al. \(2012\)](#), we use an infalling radial velocity field $v_r = \sqrt{2GM/r}$ for a $1 M_\odot$ central star; outside of the infall radius r_{infall} , the envelope is assumed to be static (i.e., $v_r = 0$). The output of RATRAN is a datacube (dimensions R.A., Decl., and radial velocity) of molecular line emission for each emission line under consideration.

To synthesize the observed single-dish spectra, we use the MIRIAD software package ([Sault et al. 1995](#)) to appropriately extract information from the RATRAN-produced datacubes. By convolving with the telescope beam profile at each frequency, and extracting the emission corresponding to the appropriate pointing offset, we produce synthetic spectra that are faithful to what would be observed with the given observational setup. In this step, we carefully observe the different offset pointings of the ground-based TIMASSS data (pointed at IRAS 16293B, located $5''$ from source A), the APEX data (pointed directly at source A), and the *Herschel* data (pointed halfway between sources A and B, i.e., $2.5''$ from source A). Following [Coutens et al. \(2012\)](#), we assume that our spherical model is centered on source A, the more massive of the two components. Finally, we resample the synthetic spectra to the velocity sampling of the observed data.⁵

4.5. Fitting

Our model fitting procedure uses a Markov chain Monte Carlo (MCMC) method. The specific MCMC implementation we use is the “emcee” package ([Foreman-Mackey et al. 2013a,b](#)), a Python implementation of the affine-invariant MCMC sampler proposed by [Goodman & Weare \(2010\)](#). The advantage of this MCMC approach is that it yields a posterior probability distribution of model parameters from which we can estimate uncertainties in the best-fit model parameters. A review of Markov Chain Monte Carlo techniques and their use in astrophysics has been recently presented by [Hogg & Foreman-Mackey \(2018\)](#).

To compare the observed data to the model spectra, we compute the following χ^2 statistic for each set of model parameters X_{in} , X_{out} , T_{jump} :

$$\chi^2 = \sum_{i=1}^N \sum_{j=1}^{n_{\text{chan}}} \frac{(T_{\text{data},i,j} - T_{\text{model},i,j})^2}{\text{rms}_i^2 + (\text{Cal}_i \times T_{\text{data},i,j})^2} \quad (3)$$

for N lines (each designated i), n_{chan} channels per line (each designated j). The observed intensity in channel j of line i of the data and model is designated $T_{\text{data},i,j}$ and $T_{\text{model},i,j}$, respectively. The per-channel rms for each line i is designated rms_i . The calibration uncertainty, denoted Cal_i , is fixed at 15% for each line.

For the MCMC run, the corresponding log-likelihood function $\ln \mathcal{L}$ is written as:

$$\ln \mathcal{L} = K - \frac{1}{2}\chi^2 \quad (4)$$

which is maximized in the MCMC fitting procedure.⁶ We constrain the model parameters (via “flat” priors) to the following ranges: $X_{\text{in}} : 10^{-12} - 10^{-8}$, $X_{\text{out}} : 10^{-14} - X_{\text{in}}$, and $T_{\text{jump}} : 30 - 120$ K.

We ran the MCMC sampler with an ensemble of 24 walkers for 1776 steps.⁷ [Foreman-Mackey et al. \(2013a\)](#) discuss ways to assess the robustness of an MCMC run, and recommend:

1. that the “acceptance fraction” fall between 0.2 – 0.5,
2. that the autocorrelation time τ be much less than the number of ensemble steps.

We find the mean acceptance fraction for each of the walkers to be 0.633, which is slightly higher than the ideal range, but not enough to raise concern. The maximum autocorrelation time τ among the three parameters was 34.7 steps; thus, we ran the MCMC chains for a factor $51 \times$ longer than τ , indicating that this MCMC run has successfully converged. Finally, we have discarded the first 69 steps (i.e., $2 \times \tau$) of the MCMC chains as “burn-in,” to ensure that the initial walker positions do not have an effect on the results presented below.

⁴ <http://home.strw.leidenuniv.nl/~moldata/>

⁵ RATRAN does not produce hyperfine structure for the $J = 1 - 0$ line, as collisional rates for the separate hyperfine states of the $J = 1 - 0$ line of H^{13}CN are not available. Therefore, we simulate the hyperfine structure of the $J = 1 - 0$ line by distributing the total flux of the $1 - 0$ line among the three hyperfine states according to their expected flux ratios. This would be inappropriate if the H^{13}CN $J = 1 - 0$ line were highly optically thick, but as the empirical flux ratios of the hyperfine components are very near the ideal LTE case of 1:5:3, this is a reasonable approach.

⁶ As these models are highly nonlinear, we refrain from computing or reporting “reduced chi-squared” values for these model fits, following [Andrae et al. \(2010\)](#).

⁷ Using a 2015 model MacBook Pro, this model took roughly 1400 s per MCMC ensemble step; the 1776-step MCMC sampler ran for 690 hours.

4.6. Results of model fitting

We present the following “best-fit” (i.e. median) parameters for the posterior probability distribution of the H^{13}CN emission model:

$$\begin{aligned} X_{\text{in}}(\text{H}^{13}\text{CN}) &= (8.51_{-0.74}^{+0.81}) \times 10^{-10} \\ X_{\text{out}}(\text{H}^{13}\text{CN}) &= (1.82_{-0.09}^{+0.09}) \times 10^{-11} \\ T_{\text{jump}} &= 71.2_{-2.6}^{+2.4} \text{ K} \end{aligned}$$

and our best-fit model is shown in Figure 2, overplotted on the data from TIMASSS, APEX, and *Herschel*. Our quoted uncertainties are drawn from the 16th, 50th, and 84th percentile thresholds (i.e., the median value $\pm 34\%$) of the sample distributions on each parameter. (This is roughly analogous to quoting $\pm 1\sigma$ errors from a Gaussian distribution.) We show the sample distributions for each model parameter (projected into a “corner plot”) in Figure 3. From the posterior distributions, it is clear that X_{in} and T_{jump} are somewhat correlated, indicating the importance of varying these two parameters simultaneously, rather than assuming a T_{jump} from the literature. The apparently tight constraints on these parameters likely are due to the wide range of E_{up} , from 4 – 273 K (cf. Table 1), sampled in the nine observed lines.

By adopting a $^{12}\text{C}/^{13}\text{C}$ ratio of 69 ± 6 (Wilson 1999), and assuming that carbon isotopic fractionation is negligible in HCN, we therefore infer the following HCN abundances:

$$\begin{aligned} X_{\text{in}}(\text{HCN}) &= (5.87_{-0.76}^{+0.72}) \times 10^{-8} \\ X_{\text{out}}(\text{HCN}) &= (1.26_{-0.13}^{+0.13}) \times 10^{-9} \end{aligned}$$

We estimated the uncertainties on these parameters by summing in quadrature the $X(\text{H}^{13}\text{CN})$ error bars with the uncertainty on the $^{12}\text{C}/^{13}\text{C}$ ratio.

4.7. Comments, limitations, and caveats of IRAS 16293 analysis

The X_{out} which we have derived for the outer envelope closely matches the measurement presented in Schöier et al. (2002). Schöier et al. (2002) use an abundance model, fit to the $J = 4 - 3$ and $3 - 2$ lines of HCN and H^{13}CN , to measure $X(\text{H}^{13}\text{CN}) = 1.8 \times 10^{-11}$. They note that, as they sample only transitions which probe energy states below 90 K, they cannot constrain the existence of a hot core abundance jump for these species, so they limit their analysis to the colder outer envelope. They derive a $X(\text{HCN}) = 1.1 \times 10^{-9}$ (assuming $^{12}\text{C}/^{13}\text{C} = 60$). If scaled to our chosen $^{12}\text{C}/^{13}\text{C} = 69$ for equivalent comparison, this gives $X(\text{HCN}) = 1.26 \times 10^{-9}$. Their independent measurements of the outer H^{13}CN and HCN abundances are essentially identical to our measured $X_{\text{out}}(\text{H}^{13}\text{CN}) = (1.82_{-0.09}^{+0.09}) \times 10^{-11}$, and $X_{\text{out}}(\text{HCN}) = (1.26_{-0.13}^{+0.13}) \times 10^{-9}$.

Our analysis, which assumes spherical symmetry of IRAS 16293, has known limitations, but the assumption of spherical symmetry is justifiable for our scientific purposes. Jørgensen et al. (2002, 2005) discuss how certain systematic effects in protostar models, such as the assumption of spherical symmetry and the uncertainty of assumed dust properties, may cause systematic uncertainties by factors of 2 – 3 in absolute abundances. As noted in depth in Jørgensen et al. (2016), IRAS 16293 is a multiple system with a non-trivial morphology on small scales. Because we are only interested in radially averaged bulk properties of the IRAS 16293 system, the spherically symmetric approach that we have taken is sufficient. While there may be systematic issues in the absolute abundance scaling of our HCN measurement, the relative ratios of HCN/ H_2O presented in Section 5 use H_2O measurements from Coutens et al. (2012) which use the same physical model, allowing some systematic issues to cancel out in the ratio. One additional concern is that the $X(\text{H}_2\text{O})$ measurement from Coutens et al. (2012) may only be a lower limit on the water abundance, and that deviation from spherical symmetry on small scales may bias the water abundance measurement from its true value near 10^{-4} (Visser et al. 2013). We consider this issue in Section 5.1.

We omit the secondary companion, IRAS 16293B, in this model; meanwhile, the ground-based observation of the $J = 1 - 0$ line from TIMASSS (Caux et al. 2011) is centered on source B. This is not a concern for our analysis, as previous data (especially SMA and ALMA resolved images of HCN from, e.g., Takakuwa et al. 2007; Zapata et al. 2013) reveal that Source A is far brighter in molecular line and continuum emission. For the $1 - 0$ line, the half-power beam width of $29''$ comprises both sources well; this, combined with the fact that we have properly considered how the flux from source A would be diluted by the pointing offset of $5''$, effectively mitigates any errors that might arise in this analysis.

4.8. HCN sublimation temperature and binding energy

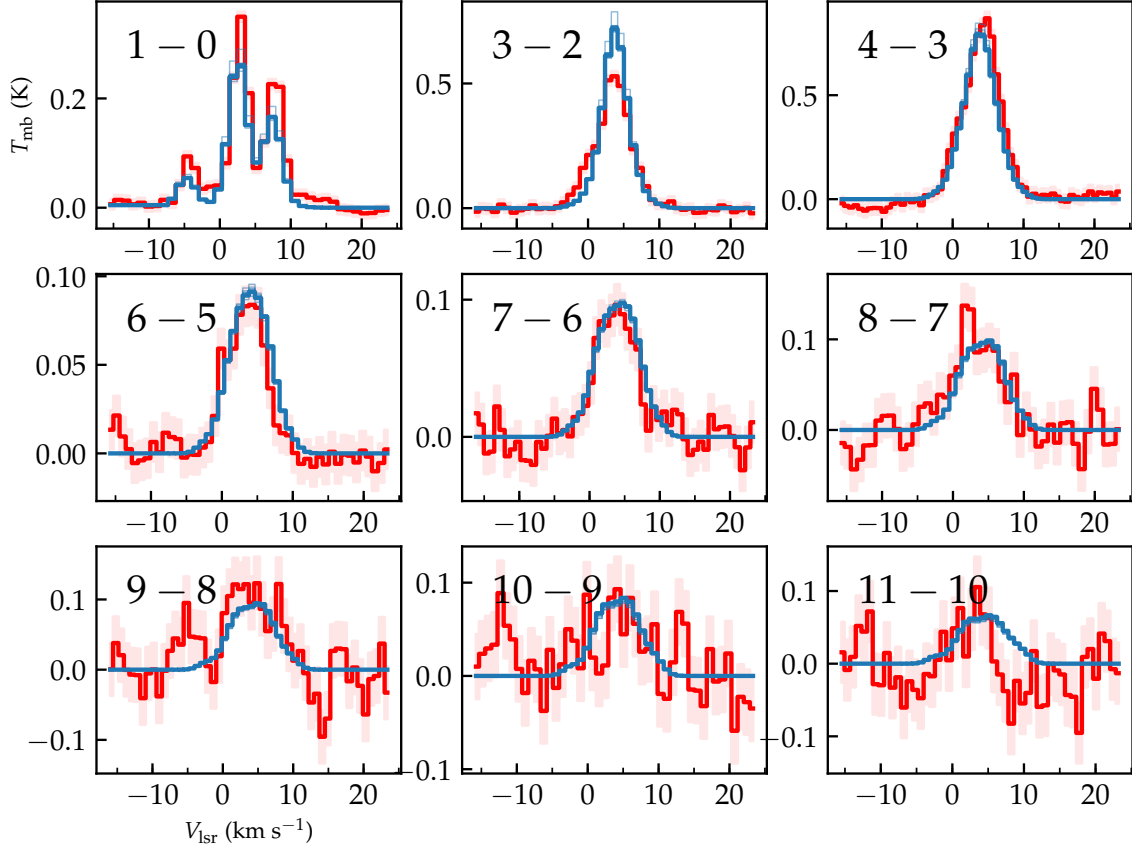


Figure 2. Comparison of observed H 13 CN spectra (red, with pink error bars) with ten representative model spectra (light blue lines) drawn from the posterior parameter distribution. The “best-fit” model (i.e., with the median values drawn from each parameter distribution) is shown with the thickest blue line. For most lines, the ten model spectra overlap too closely to distinguish.

Our observational coverage of nine H 13 CN transitions towards IRAS 16293, spanning 4–273 K in upper state energy, removes our need to assume a given T_{jump} and instead allows us to constrain it using the data. In the MCMC posterior distributions shown in Figure 3, two results from the T_{jump} posterior probability distribution are apparent: (a) the strong positive correlation between T_{jump} and X_{in} , and (b) the relatively tight constraints placed on T_{jump} given our model assumptions and the data. We discuss the consequences of these two results here.

The high positive correlation between T_{jump} and X_{in} (Pearson correlation coefficient $R = 0.82$) is not surprising, as T_{jump} effectively sets the radius of the “jump” abundance zone. For a given column density of high-temperature HCN, a higher T_{jump} (and therefore smaller sublimation region) necessitates a higher density (and therefore abundance) of those hot HCN molecules, and vice versa. Nonetheless, it does speak to the importance of estimating T_{jump} accurately in order to properly measure X_{in} . In contrast, neither $X_{\text{in}} - X_{\text{out}}$ ($R = 0.002$) nor $X_{\text{out}} - T_{\text{jump}}$ ($R = 0.23$) show meaningful correlation. As T_{jump} and X_{in} are so correlated, a change of only 20 K in the assumed T_{jump} corresponds to a $2\times$ difference in the derived X_{in} . Not all observational studies have access to *Herschel* data which constrain so many transitions and energy states of an observed molecule, but when available, using these data to simultaneously constrain T_{jump} alongside the measured abundances offers this significant advantage.

Our measurement of T_{jump} also gives information about the binding of HCN ice onto interstellar dust grains. As noted in Hollenbach et al. (2009), there is a direct connection between the freezing (or sublimation) temperature of a molecule and the value of its binding energy to dust grains. This energy is sometimes referred to as the adsorption or desorption energy, and denoted E_{B} , E_{ads} , or E_{D} . The binding energy of HCN onto dust grains is poorly constrained, as laboratory measurements involving cyanide molecules (including the temperature programmed desorption experiments used to measure binding energies) are difficult to carry out safely and accurately. Previous estimates of HCN’s binding energy range widely: 1760 K (Hasegawa & Herbst 1993), 1722 K (Bergin et al. 1995), 2050 K (Garrod & Herbst 2006, as listed in the fifth release of the UMIST Database for Astrochemistry, McElroy et al. 2013), 3370 – 3610 K (Noble

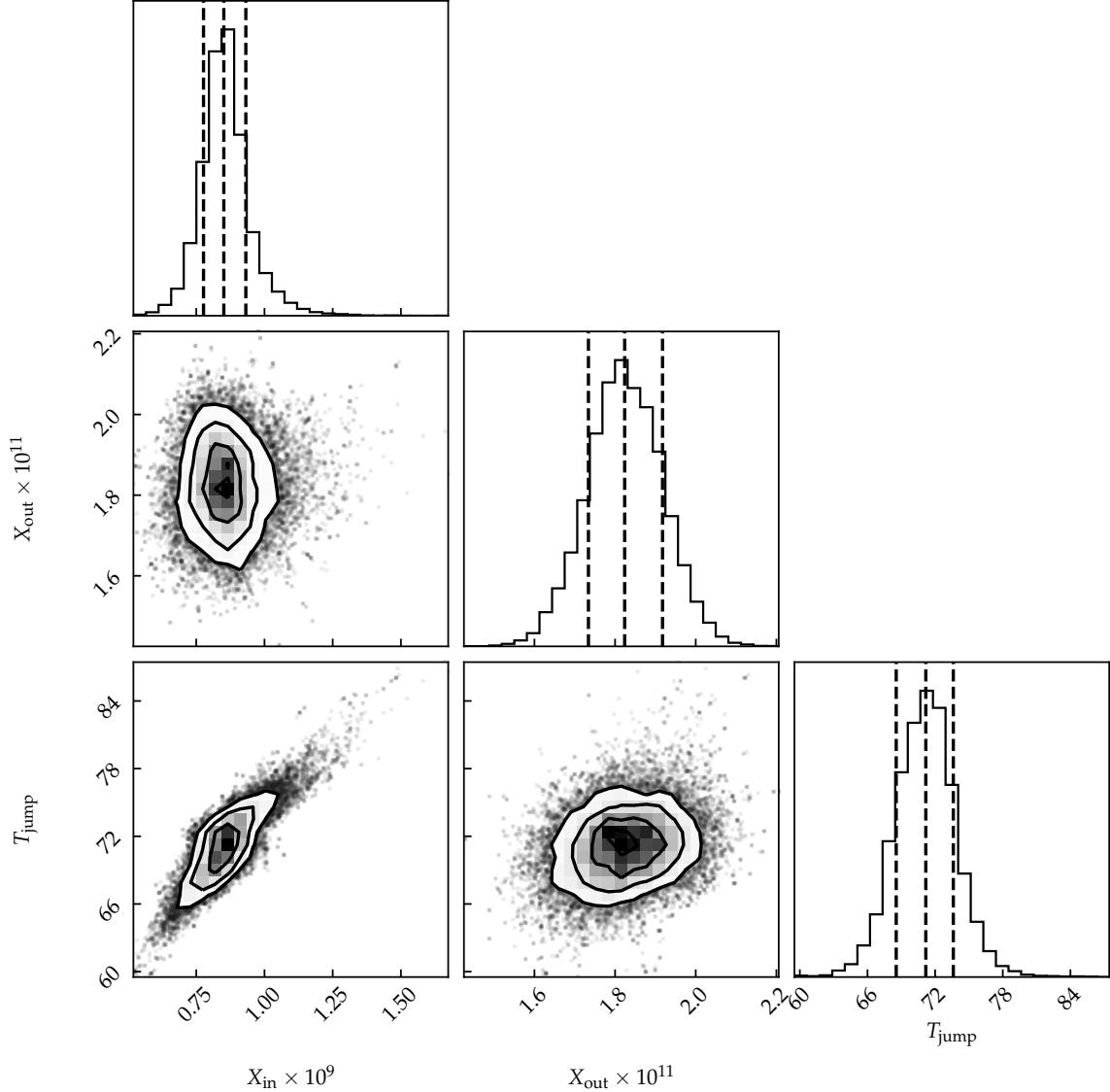


Figure 3. Corner plot of the posterior probability distributions projected into one and two dimensions along different parameter axes. Created with “corner.py” (Foreman-Mackey 2016).

et al. 2013), 4700 K (Szóri & Jedlovszky 2014), 2460 – 6974 K (Bertin et al. 2017), and 3700 K (Wakelam et al. 2017, as listed in KIDA, the Kinetic Database for Astrochemistry, Wakelam et al. 2012). This spread of binding energies corresponds to a T_{jump} range of 30 – 122 K under typical conditions.

Our derived T_{jump} allows us to make a prediction for the binding energy of HCN onto astronomical dust grains. By rewriting Equation 5 from Hollenbach et al. (2009), which is itself derived from the Polanyi-Wigner equation (Polanyi & Wigner 1925), we can express the binding energy in terms of the jump temperature as well as several other terms:

$$\frac{E_{\text{ads}}(\text{HCN})}{k} = T_{f,\text{HCN}} \times \left[57 + \ln \left[\left(\frac{N_{s,\text{HCN}}}{10^{15} \text{ cm}^{-2}} \right) \left(\frac{\nu_{\text{HCN}}}{10^{13} \text{ s}^{-1}} \right) \left(\frac{1 \text{ cm}^{-3}}{n_{\text{HCN}}} \right) \left(\frac{10^4 \text{ cm s}^{-1}}{v_{\text{HCN}}} \right) \right] \right] \quad (5)$$

with $T_{f,\text{HCN}}$ standing in for T_{jump} , $N_{s,\text{HCN}}$ the number of adsorption sites per cm^2 , n_{HCN} the number density of HCN in the gas phase, v_{HCN} its thermal speed. To saturate a single-molecule monolayer of ice, a gas-phase abundance of $\sim 10^{-6}$ relative to H_2 is typically needed; as the HCN abundance is roughly an order of magnitude below this, we take $N_{s,\text{HCN}} = 10^{14} \text{ cm}^{-2}$, i.e., 10% of available sites. We calculate the vibrational frequency $\nu_{\text{HCN}} = 5.27 \times 10^{13} \text{ s}^{-1}$. At the radius in our model at which $T = T_{\text{jump}}$, the number density $n_{\text{HCN}} = 4.9 \text{ cm}^{-3}$, and the thermal speed $v_{\text{HCN}} = 2.37 \times 10^4 \text{ cm s}^{-1}$.

We predict a binding energy $E_{\text{ads}}(\text{HCN})/k = 3840 \pm 140 \text{ K}$, given the derived $T_{\text{jump}} = 71.2_{-2.6}^{+2.4} \text{ K}$ and the physical

Table 3. Comparisons of N/H₂O ratios between protostars, comets, and ISM dust

	Protostellar sources ^a		Cometary sources ^b	ISM dust ^c
	IRAS 16293	Orion KL		
HCN/H ₂ O	0.05 – 2.0%	0.10 ± 0.06 %	0.1 – 0.6 %	...
organic N/H ₂ O	...	0.13 ± 0.07 %	0.1 – 0.9 %	...
NH ₃ /H ₂ O	...	0.12 – 0.92 %	0.4 – 1.8 %	...
total N ices	0.5 – 2.7 %	...
N/H ₂ O (dust)	5 – 24 %	≲ 19 ± 12 %

NOTE—All values given as percentages (%) relative to H₂O.

^aBased on this work, [Coutens et al. \(2012\)](#), [Neill et al. \(2013b\)](#), and [Crockett et al. \(2014b\)](#).

^bBased on [Mumma & Charnley \(2011\)](#) and [Wyckoff et al. \(1991\)](#).

^cBased on [Jensen et al. \(2007\)](#), [Whittet \(2010\)](#); [Whittet et al. \(2013\)](#), and [Nieva & Przybilla \(2012\)](#).

conditions (density, temperature, and gas-phase HCN abundance) at the corresponding radius in the envelope model. As E_{ads} depends linearly on T_{jump} but only on the logarithm of the other terms in Equation 5, we assume that uncertainties in T_{jump} dominate in contributing to uncertainties in E_{ads} .

We note that this modeling experiment was not designed to place firm constraints on the HCN binding energy, and we have not carefully investigated the sensitivity of this prediction on the various model parameters (especially including those which we consider “fixed”, such as the stellar luminosity and the physical envelope structure). Careful use of this result should be observed.

5. DISCUSSION: ON THE ORIGINS OF COMETARY NITROGEN

Previous work (e.g. [Bergin et al. 2015](#); [Füri & Marty 2015](#); [Alexander et al. 2017](#)) has suggested that refractory carbonaceous grains and molecular ices are the precursors to the nitrogen seen in the Earth’s cometary and meteoritic building blocks. In this study we have measured the nitrogen content in organic ices towards protostars at an early stage of planet formation, which offers an opportunity to compare these measurements to a late stage of planet formation. Specifically, we can compare to the ice and refractory contents of solar system comets, which are considered a relatively pristine reservoir of the materials available to the young solar system during planetary assembly (e.g., [Charnley & Rodgers 2008](#)). Through this comparison, we can explore whether we can identify (or rule out) the original source(s) of nitrogen provided to these bodies. In this section, we make use of two ratios to explore this topic: the N/H₂O ratio (to trace the bulk nitrogen), and the ¹⁴N/¹⁵N ratio (to discern between different origin populations).

The nature of nitrogen in cometary matter, as revealed by studies of material from comets Halley ([Kissel & Krueger 1987](#)), 81P/Wild 2 ([Sandford et al. 2006](#), and other references compiled in [Alexander et al. 2017](#)), and 67P/Churyumov-Gerasimenko ([Fray et al. 2016](#)), indicates that the nitrogen-bearing organic and refractory matter in comets has close isotopic and mineralogical similarities to that seen in interplanetary dust particles (IDPs) and the insoluble organic matter (IOM) in carbonaceous chondrites ([Alexander et al. 2007](#)). Further, these similarities suggest a genetic relationship between chondritic, IDP, and cometary organic matter ([Füri & Marty 2015](#); [Alexander et al. 2017](#)).

5.1. Bulk nitrogen

Central to this investigation is the question of which primordial sources of nitrogen has a high enough abundance to account for the nitrogen content of solar system planetesimals. Here we consider either molecular ices or refractory dust as these primordial nitrogen reservoirs. To compare the bulk nitrogen content of various bodies (protostars, comets, and interstellar dust), we use water (H₂O) as a standard. As the most abundant interstellar and cometary volatile species, H₂O is measurable in all of these systems. Comparing against an H₂O standard allows us to explore the connections among each of these stages. In this work we have identified N/H₂O ratios in protostars, in comets, and in interstellar dust. These are compiled in Table 3. While molecular ratios are commonly reported relative to H₂O in cometary ices, this work represents the first use of N/H₂O ratios to trace the bulk nitrogen content across

protostars, comets, and interstellar dust.

Water abundances have been measured in these protostellar environments by [Neill et al. \(2013b\)](#) for Orion KL, and [Coutens et al. \(2012\)](#) for IRAS 16293; in each case, measured using nearly identical data and techniques as those used to derive HCN abundances in this work. We focus our attention on the warm and hot “inner” environments of each protostellar system. As summarized in Table 3, the HCN/H₂O abundance in Orion KL is 0.10 ± 0.06 %, while all organic N carriers together yield an N/H₂O ratio of 0.13 ± 0.07 %. For NH₃, the wide abundance range allowed by [Gong et al. \(2015\)](#) gives a range of NH₃/H₂O values of 0.12 – 0.92%.

In IRAS 16293, we derive an HCN/H₂O ratio in the inner envelope of 1.2 ± 0.8 % when considering the H₂O abundance from [Coutens et al. \(2012\)](#) at face value. However, water abundances measured in the inner envelopes of protostars may suffer from systematic issues related to the assumption of spherical symmetry, as noted in depth by [Visser et al. \(2013\)](#), who studied H₂O in the Class 0 protostar NGC1333-IRAS2A. [Visser et al.](#) find that a spherically symmetric model for the inner 100 AU fails to reproduce the observed emission from many lines, and that a disk or proto-disk is needed to account for the discrepancy; one implication of this geometric modification is a substantially higher water abundance, likely near 10^{-4} relative to H₂, as predicted by some theoretical studies such as [Rodgers & Charnley \(2003\)](#). The comparison of ALMA data between NGC1333-IRAS2A and IRAS 16293 indicates that IRAS 16293 itself has a 30-times-higher H₂O column density on scales revealed by ALMA ([Persson et al. 2013](#); [Visser et al. 2013](#)), indicating that its abundances are also likely affected by this issue. These geometric effects are most severe at the smallest scales, where the sublimation zone of H₂O lies, so H₂O is more affected by this issue than HCN. We therefore consider the warm inner H₂O abundance of IRAS 16293 to be somewhere in the range of $5 \times 10^{-6} - 10^{-4}$; when uncertainties in the HCN abundance are folded in, this yields an HCN/H₂O ratio 0.05 – 2.0%, with some preference for the lower end of this range.

The cometary abundances of many molecular species are compiled in [Mumma & Charnley \(2011\)](#) relative to H₂O. The most abundant and second-most-abundant nitrogen-bearing ices in comets are NH₃ and HCN, respectively ([Mumma & Charnley 2011](#)). Cometary NH₃ ice has an abundance of $\sim 0.4 - 1.8$ % relative to H₂O ice. HCN, the next largest contributor, has an abundance of 0.1 – 0.6% relative to H₂O. Other, less-abundant species sum to at most 0.3%, giving a total N abundance in ices of 0.5 – 2.7%. We find that the protostellar abundances for molecular N-bearing ices are of roughly the same order of magnitude as the cometary ice abundances. This suggests that the nitrogen-bearing molecular ices already present on dust grain surfaces in the protostellar stage may be the direct progenitors to the nitrogenic molecular ices found in comets, as suggested previously by numerous other studies (cf. [Mumma & Charnley 2011](#), and references therein).

Only a small portion of cometary nitrogen is contained in molecular ices, however. [Wyckoff et al. \(1991\)](#) measured the ratio of nitrogen in the dust to gas in Comet 1P/Halley to be 90:10, i.e., only 10% of Halley’s nitrogen is in the gas, with the vast majority in dust. Measurements by the Rosetta probe indicate that Comet 67P also has much more N in dust: results from COSAC and Philae ([Goesmann et al. 2015](#); [Wright et al. 2015](#)), COSIMA ([Fray et al. 2017](#)), and ROSINA ([Le Roy et al. 2015](#)) all confirm that the dust of 67P is more N-rich than the gas. Based on these studies of comets Halley and 67P, we therefore estimate the total nitrogen content in the typical comet as compiled by [Mumma & Charnley \(2011\)](#), by multiplying the range of N-ices/H₂O abundances by 10×. We estimate that the N/H₂O in dust in comets is 5 – 24%, and the bulk N/H₂O ratio in comets is 5 – 27%. Therefore, the nitrogen in molecular ices measured in protostars is an order of magnitude or more too low to account for the total nitrogen content of comets.

In principle, the most volatile forms of nitrogen (especially N₂) should contain the majority of interstellar nitrogen at the beginning of the planet formation process (see, e.g., [Schwarz & Bergin 2014](#)). However, we can exclude these more volatile forms of nitrogen as contributors to cometary nitrogen, based on chemical and physical principles. It would be very surprising if these species were able to undergo solid-state chemistry and contribute to chemical complexity, given their low sublimation temperatures and binding energies (as shown in Table 4) and the slow rates at which gas-phase chemistry proceeds. The molecular species NO and NS also likely have binding energies too low to permit freeze-out and its subsequent chemical enrichment.

An additional source of nitrogen for comets may exist: refractory nitrogen within interstellar dust. Nitrogen has not been detected directly in ISM dust, and it is difficult to observationally constrain the presence of nitrogen in carbon-rich dust via spectroscopic observations ([Jones 2016](#)). Nonetheless, an upper limit on nitrogen’s abundance can be inferred from measurements of N in interstellar gas, specifically via the depletion of N in diffuse ISM gas relative to the cosmic abundance of nitrogen atoms. [Nieva & Przybilla \(2012\)](#) measure the present-day cosmic abundance of nitrogen (relative to hydrogen) in the local Universe to be N/H = 62 ± 6 ppm. [Jensen et al. \(2007\)](#) measure the abundance of N I gas along multiple sight lines of the diffuse ISM to be 51 ± 4 ppm. Based on these numbers, the nitrogen depletion in the diffuse ISM is 11 ± 7 ppm. This number may represent depletion into different types of

Table 4. Binding energies and sublimation temperatures for simple N-bearing species

Species	E_B/k (K)	T_{jump} (K)
N	720 ± 216	13 ± 4
N ₂	1100 ± 330	19 ± 6
NO	1600 ± 480	28 ± 8
NS	1900 ^a	33
HCN	3700 ± 1100	65 ± 19
	or 3840 ± 140 ^b	or 70 ± 2
NH ₃	5500 ± 1650	96 ± 29

^aGarrod & Herbst (2006), as listed in the KIDA database (Wakelam et al. 2012)

^bThis work; see §4.8

NOTE—Sublimation temperatures T_{jump} calculated using typical ISM conditions following Hollenbach et al. (2009). All binding energies from Wakelam et al. (2017), as listed in the KIDA database (Wakelam et al. 2012), unless otherwise noted. In all cases, the binding surface is assumed to be H₂O ice.

nitrogen sinks, such as formation of N₂ molecules or other species, but this depletion is measured in low-extinction (low A_V) environments where molecular N₂ would be rapidly destroyed by interstellar ultraviolet radiation. Therefore, the most likely interpretation is nitrogen depletion into refractory dust grains. In any case, the 11 ± 7 ppm is an upper limit on the available nitrogen in interstellar refractory dust. Whittet (2010) and Whittet et al. (2013) show that the abundance of oxygen atoms within ices on interstellar dust grains is 116 ppm (relative to H), and the solar O/H abundance is 457 ppm. Of this, about 50–60% of the oxygen atoms are in H₂O, with the rest in CO, and CO₂. Taking 50% of the 116 ppm as H₂O ice yields an H₂O ice-on-dust abundance of 58 ppm versus H in the ISM. Dividing the refractory N value by this H₂O on dust, we present an upper limit of $19 \pm 12\%$ on refractory nitrogen in the ISM relative to water. This upper limit is comparable to the bulk nitrogen abundance in comets. Because there are no other apparent sources of nitrogen to comets with high enough abundance, we suggest that interstellar dust is the likely origin of the majority of cometary nitrogen.

5.2. ¹⁵N enrichment

In the previous subsection we suggested that the bulk of cometary nitrogen may be inherited from interstellar dust, as molecular ices do not have a high enough abundance relative to water to provide the majority of cometary nitrogen. To further explore the origins of cometary nitrogen, we turn to the isotopic signature of ¹⁵N. Isotopic ratios such as the ¹⁴N/¹⁵N ratio are commonly used to trace populations of material, as the isotopic ratio can be robust to physical processes and persist through time. In the solar system, the nitrogen in planetesimals is significantly more ¹⁵N-rich than the Sun and the local interstellar medium: the solar value ¹⁴N/¹⁵N ratio is 441, while planetesimals have values ranging from 200, 50, or 140 (Füri & Marty 2015, for bulk chondrites, chondrite hot spots, and comets, respectively). Direct measurements of ¹⁴N/¹⁵N in the dust particles of Comet 81P/Wild 2 show a range of ¹⁴N/¹⁵N values from $\sim 180 - 270$ (McKeegan et al. 2006). The present-day Earth itself has a sub-solar ¹⁴N/¹⁵N ratio of 272 (Anders & Grevesse 1989).

The common interpretation of the ¹⁵N enrichment in comets and other bodies is that it originates in the low-temperature molecular chemistry that occurs in either interstellar clouds or the early phases of star and planet formation (Charnley & Rodgers 2008; Wörström et al. 2012; Hily-Blant et al. 2013; Füri & Marty 2015; Bockelée-Morvan et al. 2015; Alexander et al. 2017). ¹⁵N fractionation is consistently observed in N-bearing molecular ices (amines & nitriles) in dense star-forming gas (Hily-Blant et al. 2013; Wampfler et al. 2014, as well as this study). Hily-Blant et al.

(2017) present evidence for multiple nitrogen reservoirs within forming solar systems, with distinct isotopic signatures. The similar N/H₂O abundances for N-bearing molecules around protostars derived in this work, and in cometary ices, further lends support to the interpretation that ices are the ¹⁵N donor to comets. However, recent work by Roueff et al. (2015) and Wirström & Charnley (2018) indicates that, when updated reaction rates and more sophisticated quantum-chemical computations are included, the current chemical networks cannot reproduce the observed ¹⁵N enrichments in several N-bearing molecules, leaving room for exploration of the origins of ¹⁵N in the dense ISM. Regardless, observations clearly indicate that ISM chemistry can produce ¹⁵N enrichments in distinct chemical families (e.g. nitriles).

Thus, while substantial evidence supports a molecular ice origin for ¹⁵N in comets, we ask whether a dust origin be ruled out entirely. This question is especially important to resolve given the large contribution of N from dust, as a small ¹⁵N contribution from dust would matter more than a large ¹⁵N contribution from ices. Unfortunately, the ¹⁵N content of ISM dust is both unknown and totally unconstrained by observation; this requires us to rely on indirect evidence to investigate where cometary ¹⁵N originates. Most of the nitrogen in interstellar dust would be expected to be contained in carbonaceous (rather than silicate) grains. The formation of carbonaceous dust, discussed by Chiar et al. (2013), occurs in ~ 1000 K environments that do not encourage chemical fractionation of nitrogen. The incorporation of nitrogen into hydrocarbon dust, discussed by Jones (2016), also would not be expected to enrich ¹⁵N over ¹⁴N. The cores of interstellar dust grains consist of presolar stardust that form directly from stellar ejecta (Clayton & Nittler 2004; Chiar et al. 2013). While the ¹⁴N/¹⁵N ratio of interstellar dust is unknown, individual presolar stardust grains can survive planetesimal formation intact and are amenable to isotopic study. These stardust grains, by virtue of their localized formation, inherit isotopic ratios directly from the nucleosynthetic and stellar evolutionary processes in their parent star. Presolar stardust grains, particularly SiC-X, graphite, and Si₃N₄, were studied by Clayton & Nittler (2004). Graphite grains typically have the same nitrogen isotopic ratio as the Sun, but SiC-X and Si₃N₄ grains are ¹⁵N-rich, with ¹⁴N/¹⁵N values as low as 20 in some cases. Clayton & Nittler (2004) discuss how these high ¹⁵N values may be linked to the dust formation and nucleosynthesis processes in supernovae. In a related process, nova eruptions may be partly responsible for the gradual rise of ¹⁵N enrichment in a galaxy over time (Romano et al. 2017).

Additional evidence comes from analysis of organic matter within carbonaceous chondrites. Notably, the ¹⁵N hotspots in chondrites are not typically correlated with mineral rims or individual silicate grains (Alexander et al. 2017), although an instance of ¹⁵N enrichment near a supernova silicate grain in an IDP was noted by Messenger et al. (2005). The variable ¹⁵N enrichment (concentrated in ¹⁵N-rich “hotspots”) might be consistent with an origin in diverse, heterogeneous stardust grains which each carry a different degree of ¹⁵N enrichment. This may also be consistent with how D and ¹⁵N hotspots do not exactly correlate: ¹⁵N hotspots are often associated with ¹³C isotopic anomalies, while D hotspots do not co-vary with ¹³C (Alexander et al. 2017). These isotopic co-variations may also just be the result of chemistry: Wirström et al. (2012) note that for HCN and HNC, the reactions that lead to ¹⁵N enrichment do not correlate with the most extreme D enrichment.

If there exist thermal, aqueous, or chemical processes that can transport ¹⁵N out of stardust grains and into organic matter during the formation of comets and other bodies, then we may not yet be able to rule out a dust origin for ¹⁵N in these planetesimal bodies. Otherwise, most of the available evidence is in favor of a molecular ice origin, although recent work in chemical models indicates that further theoretical and laboratory work is needed to understand the precise reactions that lead to ¹⁵N enrichment. In this framework, molecular ices are the donor of ¹⁵N to protoplanetary solid bodies — and ultimately to the Earth. Thus, following these molecular ices allows us to astronomically trace a meaningful component of the nitrogen that later becomes a part of terrestrial worlds.

6. CONCLUSIONS

From our analysis of the nitrogen-bearing organic molecular inventories in a high-mass hot core, the HCN lines towards a low-mass protostar, and through scaling molecular abundances relative to H₂O, we present the following conclusions:

1. HCN is by far the most abundant nitrogen-bearing organic in the Orion KL Hot Core, carrying $74^{+5}_{-9}\%$ of nitrogen-in-organics.
2. The HCN abundance in the envelope of IRAS 16293–2422 exhibits a jump profile, with $X_{\text{in}} = 5.9 \pm 0.7 \times 10^{-8}$ and an outer HCN abundance $X_{\text{out}} = 1.26 \pm 0.13 \times 10^{-9}$.
3. We derive an HCN sublimation temperature $T_{\text{jump}} = 71 \pm 3$ K, from which we make an astronomically-motivated prediction that the HCN binding energy $E_B/k = 3840 \pm 140$ K.

4. The N/H₂O ratio in molecular ices seen in the inner protostellar envelopes is similar to N/H₂O in cometary ices. However, it is not high enough to account for the total N/H₂O seen in comets. While the refractory nitrogen content in interstellar dust has not been measured, its upper limit is permissive enough to account for the bulk of cometary N. Therefore, we suggest that the nitrogen contained in interstellar dust is the likely precursor to most of the N in comets.
5. The high ¹⁵N enrichment seen in cometary and meteoritic bodies has an unknown origin. Most evidence indicates that it is donated by molecular ices that underwent chemical fractionation of nitrogen isotopes, but the reactions responsible for this process are unclear. A dust origin of ¹⁵N enrichment appears unlikely but cannot be ruled out.

We thank K. Villalon for assistance with the geochemistry literature. We thank L. I. Cleaves, K. Schwarz, and S. Manigand for guidance with the molecular adsorption energy literature. We thank L. E. Kristensen for discussions about data handling and model fitting. We thank S. Massalkhi for assistance with the literature on giant stars. We thank P. Hily-Blant for discussions on the origins of nitrogen.

This material is based upon work supported by the National Science Foundation Graduate Research Fellowship Program under Grant No. 1256260 and an international travel allowance through the Graduate Research Opportunities Worldwide (GROW). This work was additionally supported by funding from NSF grants AST-1514670 as well as NASA NNX16AB48G. Any opinions, findings, and conclusions or recommendations expressed in this material are those of the author(s) and do not necessarily reflect the views of the National Science Foundation. JKJ is supported by the European Research Council (ERC) under the European Union’s Horizon 2020 research and innovation programme (grant agreement No 646908) through ERC Consolidator Grant “S4F”. Research at Centre for Star and Planet Formation is funded by the Danish National Research Foundation.

Software: This research made use of the following: Astropy, a community-developed core Python package for Astronomy (Astropy Collaboration et al. 2013; The Astropy Collaboration et al. 2018); GILDAS, a collection of software to reduce and analyze (sub)millimeter data (Pety 2005; Gildas Team 2013; Pety 2018, <http://www.iram.fr/IRAMFR/GILDAS>); Matplotlib (Hunter 2007), a Python package for generating scientific plots; “emcee” (Foreman-Mackey et al. 2013b), a Python MCMC affine-invariant sampler; “corner.py,” a Python tool to visualize corner plots of MCMC posterior distributions (Foreman-Mackey 2016); and WebPlotDigitizer (Rohatgi & ZlatanStanojevic 2017), to better access published information in the literature.

APPENDIX

A. *HERSCHEL* LINE FITTING RESULTS FOR IRAS 16293

In this Appendix, we show the detailed results of fitting the HCN, H¹³CN, and HC¹⁵N lines of IRAS 16293 from the *Herschel* data, as well as the derived properties (such as the optical depth τ) of each state that are measured from comparisons of the isotopologues. The lines and their Gaussian fits are shown in Figure A1. The fit parameters for the *Herschel* lines, as well as for the ground-based lines from Caux et al. (2011) and Wampfler et al. (2014), are presented in A1, and the properties derived from these fits are shown in A2.

Table A1. Observed lines of HCN and isotopologues towards IRAS 16293

Species & Transition	Frequency (GHz)	Telescope & Band	θ_{mb} ('')	V_0 (km s ⁻¹)	FWHM (km s ⁻¹)	peak flux (K)	$\int T_{\text{mb}} dv$ (K km s ⁻¹)
HCN J= 1 – 0	88.6316	IRAM-30m	28.4	4.46 ± 0.33	9.50 ± 0.79	1.765	21.71 ± 2.39
HCN J= 3 – 2	265.8864	APEX-1	24.3	3.72 ± 0.01	6.81 ± 0.02	9.66	27.52 ± 2.3
HCN J= 6 – 5	531.7164	HIFI 1a	40.5	3.94 ± 0.02	5.30 ± 0.07	1.072	6.04 ± 0.06
HCN J= 7 – 6	620.3041	HIFI 1b	34.7	3.96 ± 0.02	5.70 ± 0.05	0.903	5.48 ± 0.04
HCN J= 8 – 7	708.8772	HIFI 2a	30.4	3.98 ± 0.06	5.74 ± 0.15	0.776	4.74 ± 0.10
HCN J= 9 – 8	797.4337	HIFI 2b	27.0	3.97 ± 0.09	6.80 ± 0.22	0.543	3.93 ± 0.11
HCN J= 10 – 9	885.9714	HIFI 3b	24.3	3.69 ± 0.09	7.06 ± 0.24	0.531	3.99 ± 0.11

Table A1 continued on next page

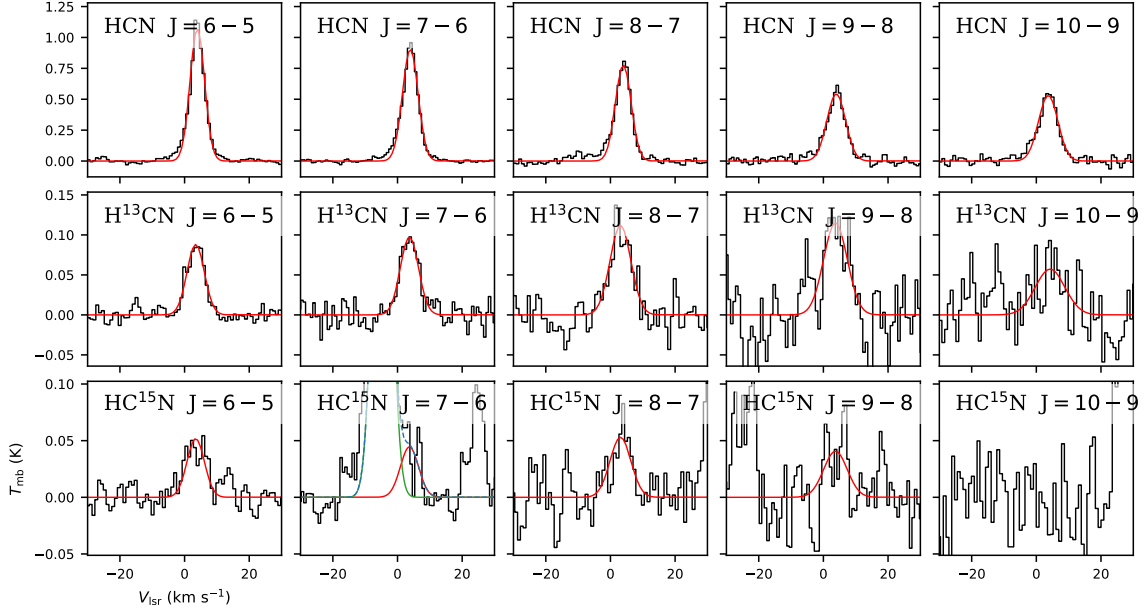


Figure A1. Gaussian fits to the HCN and isotopologue lines in the HIFI data of IRAS 16293. Smoothed to $3\times$ the resolution of the lowest HCN line. We fit the $\text{HC}^{15}\text{N } J=7-6$ line simultaneously with the blended $\text{SO } J=14-13$ line at 602.292 GHz. We consider $\text{HC}^{15}\text{N } J=10-9$ to be undetected.

Table A1 (*continued*)

Species & Transition	Frequency (GHz)	Telescope & Band	θ_{mb} ($''$)	V_0 (km s^{-1})	FWHM (km s^{-1})	peak flux (K)	$\int T_{\text{mb}} dv$ (K km s^{-1})
$\text{H}^{13}\text{CN } J=1-0$	86.3402	IRAM-30m	29.1	3.88 ± 0.09	2.91 ± 0.25	0.284	1.04 ± 0.12
$\text{H}^{13}\text{CN } J=3-2$	259.0118	APEX-1	24.3	3.75 ± 0.03	5.70 ± 0.08	0.68	3.24 ± 0.3
$\text{H}^{13}\text{CN } J=4-3$	345.3397	APEX-2	18.2	4.28 ± 0.04	6.11 ± 0.09	1.08	5.56 ± 0.8
$\text{H}^{13}\text{CN } J=6-5$	517.9698	HIFI 1a	41.6	3.44 ± 0.14	6.35 ± 0.30	0.088	0.60 ± 0.03
$\text{H}^{13}\text{CN } J=7-6$	604.2679	HIFI 1b	35.7	3.69 ± 0.20	6.62 ± 0.49	0.097	0.69 ± 0.04
$\text{H}^{13}\text{CN } J=8-7$	690.5521	HIFI 2a	31.2	3.10 ± 0.29	7.63 ± 0.69	0.112	0.91 ± 0.07
$\text{H}^{13}\text{CN } J=9-8$	776.8203	HIFI 2b	27.7	3.73 ± 0.61	8.60 ± 1.48	0.115	1.05 ± 0.15
$\text{H}^{13}\text{CN } J=10-9$	863.0706	HIFI 3b	25.0	4.27 ± 1.41	10.80 ± 3.91	0.057	0.66 ± 0.18
$\text{HC}^{15}\text{N } J=1-0$	86.0550	IRAM-30m	29.2	4.03 ± 0.18	3.51 ± 0.43	0.114	0.51 ± 0.06
$\text{HC}^{15}\text{N } J=3-2$	258.1570	APEX-1	24.3	3.71 ± 0.09	6.2 ± 0.2	0.27	1.37 ± 0.1
$\text{HC}^{15}\text{N } J=4-3$	344.2001	APEX-2	18.2	3.11 ± 0.09	6.4 ± 0.2	0.44	2.02 ± 0.3
$\text{HC}^{15}\text{N } J=6-5$	516.2615	HIFI 1a	41.8	3.44 ± 0.14	6.35 ± 0.30	0.052	0.35 ± 0.04
$\text{HC}^{15}\text{N } J=7-6$	602.2754	HIFI 1b	35.8	3.69 ± 0.20	6.62 ± 0.49	0.044	0.31 ± 0.08
$\text{HC}^{15}\text{N } J=8-7$	688.2758	HIFI 2a	31.3	3.10 ± 0.29	7.63 ± 0.69	0.053	0.43 ± 0.25
$\text{HC}^{15}\text{N } J=9-8$	774.2605	HIFI 2b	27.8	3.73 ± 0.61	8.60 ± 1.48	0.041	0.37 ± 0.11

Table A2. Derived properties of each energy state of HCN towards IRAS 16293

J_u	$\tau_{\text{H}^{13}\text{CN}}$	τ_{HCN}	$\tau_{\text{HC}^{15}\text{N}}$	$\text{H}^{13}\text{CN} / \text{HC}^{15}\text{N}$	$^{14}\text{N} / ^{15}\text{N}$
6	0.09	5.92	0.05	1.7	119
7	0.11	7.87	0.05	2.3	155

Table A2 continued on next page

Table A2 (*continued*)

J_u	$\tau_{\text{H}^{13}\text{CN}}$	τ_{HCN}	$\tau_{\text{HC}^{15}\text{N}}$	$\text{H}^{13}\text{CN} / \text{HC}^{15}\text{N}$	$^{14}\text{N} / ^{15}\text{N}$
8	0.16	10.73	0.07	2.2	151
9	0.24	16.41	0.08	3.0	210
10	0.11	7.87	—	—	—

NOTE—Derived properties for HCN and $^{14}\text{N} / ^{15}\text{N}$ assume a $^{12}\text{C} / ^{13}\text{C}$ ratio of 69 ± 6 following [Wilson \(1999\)](#).

REFERENCES

- Adams, F. C., & Shu, F. H. 1986, *ApJ*, 308, 836
- Adande, G. R., Woolf, N. J., & Ziurys, L. M. 2013, *Astrobiology*, 13, 439
- Alexander, C. M. O. ., Bowden, R., Fogel, M. L., et al. 2012, *Science*, 337, 721
- Alexander, C. M. O. ., Cody, G. D., De Gregorio, B. T., Nittler, L. R., & Stroud, R. M. 2017, *Chemie der Erde / Geochemistry*, 77, 227
- Alexander, C. M. O. ., Fogel, M., Yabuta, H., & Cody, G. D. 2007, *GeoCoA*, 71, 4380
- Anders, E., & Grevesse, N. 1989, *GeoCoA*, 53, 197
- Andrae, R., Schulze-Hartung, T., & Melchior, P. 2010, *ArXiv e-prints*, arXiv:1012.3754
- Astropy Collaboration, Robitaille, T. P., Tollerud, E. J., et al. 2013, *A&A*, 558, A33
- Bacmann, A., Caux, E., Hily-Blant, P., et al. 2010, *A&A*, 521, L42
- Bergin, E. A., Blake, G. A., Ciesla, F., Hirschmann, M. M., & Li, J. 2015, *Proceedings of the National Academy of Sciences*, 112, 8965
- Bergin, E. A., Cleeves, L. I., Crockett, N., & Blake, G. A. 2014, *Faraday Discussions*, 168, arXiv:1405.7394
- Bergin, E. A., Langer, W. D., & Goldsmith, P. F. 1995, *ApJ*, 441, 222
- Bergin, E. A., Phillips, T. G., Comito, C., et al. 2010, *A&A*, 521, L20
- Bertin, M., Doronin, M., Fillion, J.-H., et al. 2017, *A&A*, 598, A18
- Bockelée-Morvan, D., Calmonte, U., Charnley, S., et al. 2015, *SSRv*, 197, 47
- Bonal, L., Huss, G. R., Krot, A. N., et al. 2010, *GeoCoA*, 74, 6590
- Briani, G., Gounelle, M., Marrocchi, Y., et al. 2009, *Proceedings of the National Academy of Science*, 106, 10522
- Brinch, C., Jørgensen, J. K., & Hogerheijde, M. R. 2009, *A&A*, 502, 199
- Calcutt, H., Jørgensen, J. K., Müller, H. S. P., et al. 2018a, *ArXiv e-prints*, arXiv:1804.09210
- Calcutt, H., Fiechter, M. R., Willis, E. R., et al. 2018b, *ArXiv e-prints*, arXiv:1807.02909
- Caux, E., Kahane, C., Castets, A., et al. 2011, *A&A*, 532, A23
- Cazaux, S., Tielens, A. G. G. M., Ceccarelli, C., et al. 2003, *ApJL*, 593, L51
- Ceccarelli, C., Bacmann, A., Boogert, A., et al. 2010, *A&A*, 521, L22
- Cernicharo, J. 2012, in *EAS Publications Series*, Vol. 58, *EAS Publications Series*, ed. C. Stehlé, C. Joblin, & L. d’Hendecourt, 251–261
- Cernicharo, J., Kisiel, Z., Tercero, B., et al. 2016, *A&A*, 587, L4
- Chandler, C. J., Brogan, C. L., Shirley, Y. L., & Loinard, L. 2005, *ApJ*, 632, 371
- Charnley, S. B., & Rodgers, S. D. 2008, *SSRv*, 138, 59
- Chiar, J. E., Tielens, A. G. G. M., Adamson, A. J., & Ricca, A. 2013, *ApJ*, 770, 78
- Clayton, D. D., & Nittler, L. R. 2004, *Origin and Evolution of the Elements*, 297
- Colzi, L., Fontani, F., Rivilla, V. M., et al. 2018, *MNRAS*, 478, 3693
- Coutens, A., Vastel, C., Caux, E., et al. 2012, *A&A*, 539, A132
- Crimier, N., Ceccarelli, C., Maret, S., et al. 2010, *A&A*, 519, A65
- Crockett, N. R., Bergin, E. A., Neill, J. L., et al. 2014a, *ApJ*, 781, 114
- . 2015, *ApJ*, 806, 239
- Crockett, N. R., Bergin, E. A., Wang, S., et al. 2010, *A&A*, 521, L21
- Crockett, N. R., Bergin, E. A., Neill, J. L., et al. 2014b, *ApJ*, 787, 112
- Dullemond, C. P., van Zadelhoff, G. J., & Natta, A. 2002, *A&A*, 389, 464
- Dumouchel, F., Faure, A., & Lique, F. 2010, *MNRAS*, 406, 2488
- Dzib, S. A., Ortiz-León, G. N., Hernández-Gómez, A., et al. 2018, *A&A*, 614, A20
- Endres, C. P., Schlemmer, S., Schilke, P., Stutzki, J., & Müller, H. S. P. 2016, *Journal of Molecular Spectroscopy*, 327, 95
- Foreman-Mackey, D. 2016, *corner.py: corner.py v1.0.2*, , , doi:10.5281/zenodo.45906
- Foreman-Mackey, D., Hogg, D. W., Lang, D., & Goodman, J. 2013a, *PASP*, 125, 306
- Foreman-Mackey, D., Conley, A., Meierjürgen Farr, W., et al. 2013b, *emcee: The MCMC Hammer*, *Astrophysics Source Code Library*, , , ascl:1303.002
- Fray, N., Bardyn, A., Cottin, H., et al. 2016, *Nature*, 538, 72
- . 2017, *MNRAS*, 469, S506
- Füri, E., & Marty, B. 2015, *Nature Geoscience*, 8, 515
- Furuya, K., & Aikawa, Y. 2018, *ApJ*, 857, 105
- Furuya, K., & Persson, M. V. 2018, *MNRAS*, 476, 4994
- Furuya, K., Watanabe, Y., Sakai, T., Aikawa, Y., & Yamamoto, S. 2018, *A&A*, 615, L16
- Garrod, R. T., & Herbst, E. 2006, *A&A*, 457, 927
- Gildas Team. 2013, *GILDAS: Grenoble Image and Line Data Analysis Software*, *Astrophysics Source Code Library*, , , ascl:1305.010
- Goesmann, F., Rosenbauer, H., Bredehöft, J. H., et al. 2015, *Science*, 349, <http://science.sciencemag.org/content/349/6247/aab0689.full.pdf>
- Gong, Y., Henkel, C., Thorwirth, S., et al. 2015, *A&A*, 581, A48
- Goodman, J., & Weare, J. 2010, *Communications in applied mathematics and computational science*, 5, 65

- Guzmán, V. V., Öberg, K. I., Huang, J., Loomis, R., & Qi, C. 2017, *ApJ*, 836, 30
- Hasegawa, T. I., & Herbst, E. 1993, *MNRAS*, 261, 83
- Hily-Blant, P., Bonal, L., Faure, A., & Quirico, E. 2013, *Icarus*, 223, 582
- Hily-Blant, P., Magalhaes, V., Kastner, J., et al. 2017, *A&A*, 603, L6
- Hily-Blant, P., Maret, S., Bacmann, A., et al. 2010, *A&A*, 521, L52
- Hogerheijde, M., & van der Tak, F. 2000a, *RATRAN: Radiative Transfer and Molecular Excitation in One and Two Dimensions*, *Astrophysics Source Code Library*, , , ascl:0008.002
- Hogerheijde, M. R., & van der Tak, F. F. S. 2000b, *A&A*, 362, 697
- Hogg, D. W., & Foreman-Mackey, D. 2018, *ApJS*, 236, 11
- Hollenbach, D., Kaufman, M. J., Bergin, E. A., & Melnick, G. J. 2009, *ApJ*, 690, 1497
- Hunter, J. D. 2007, *Computing In Science & Engineering*, 9, 90
- Jacobsen, S. K., Jørgensen, J. K., van der Wiel, M. H. D., et al. 2017, *ArXiv e-prints*, arXiv:1712.06984
- Jensen, A. G., Rachford, B. L., & Snow, T. P. 2007, *ApJ*, 654, 955
- Jones, A. P. 2016, *Royal Society Open Science*, 3, 160221
- Jørgensen, J. K., Bourke, T. L., Nguyen Luong, Q., & Takakuwa, S. 2011, *A&A*, 534, A100
- Jørgensen, J. K., Schöier, F. L., & van Dishoeck, E. F. 2002, *A&A*, 389, 908
- . 2005, *A&A*, 435, 177
- Jørgensen, J. K., van der Wiel, M. H. D., Coutens, A., et al. 2016, *A&A*, 595, A117
- Kahane, C., Jaber Al-Edhari, A., Ceccarelli, C., et al. 2018, *ApJ*, 852, 130
- Kissel, J., & Krueger, F. R. 1987, *Nature*, 326, 755
- Knauth, D. C., Andersson, B.-G., McCandliss, S. R., & Moos, H. W. 2003, *ApJL*, 596, L51
- Le Roy, L., Altwegg, K., Balsiger, H., et al. 2015, *A&A*, 583, A1
- Ligterink, N. F. W., Coutens, A., Kofman, V., et al. 2017, *MNRAS*, 469, 2219
- Loinard, L., Torres, R. M., Mioduszewski, A. J., & Rodríguez, L. F. 2008, *ApJL*, 675, L29
- Looney, L. W., Mundy, L. G., & Welch, W. J. 2000, *ApJ*, 529, 477
- Lykke, J. M., Coutens, A., Jørgensen, J. K., et al. 2017, *A&A*, 597, A53
- Maret, S., Ceccarelli, C., Caux, E., et al. 2004, *A&A*, 416, 577
- Marty, B. 2012, *Earth and Planetary Science Letters*, 313, 56
- Marty, B., Zimmermann, L., Burnard, P. G., et al. 2010, *GeoCoA*, 74, 340
- Marty, B., Zimmermann, L., Pujol, M., Burgess, R., & Philippot, P. 2013, *Science*, 342, 101
- Marty, B., Avicé, G., Sano, Y., et al. 2016, *Earth and Planetary Science Letters*, 441, 91
- Marty, B., Altwegg, K., Balsiger, H., et al. 2017, *Science*, 356, 1069
- McElroy, D., Walsh, C., Markwick, A. J., et al. 2013, *A&A*, 550, A36
- McKeegan, K., Aléon, J., Bradley, J., et al. 2006, *Science*, 314, 1724
- Messenger, S., Keller, L. P., & Lauretta, D. S. 2005, *Science*, 309, 737
- Morbidelli, A., Lunine, J. I., O'Brien, D. P., Raymond, S. N., & Walsh, K. J. 2012, *Annual Review of Earth and Planetary Sciences*, 40, 251
- Müller, H. S. P., Thorwirth, S., Roth, D. A., & Winnewisser, G. 2001, *A&A*, 370, L49
- Mumma, M. J., & Charnley, S. B. 2011, *ARA&A*, 49, 471
- Neill, J. L., Crockett, N. R., Bergin, E. A., Pearson, J. C., & Xu, L.-H. 2013a, *ApJ*, 777, 85
- Neill, J. L., Wang, S., Bergin, E. A., et al. 2013b, *ApJ*, 770, 142
- Nieva, M.-F., & Przybilla, N. 2012, *A&A*, 539, A143
- Noble, J. A., Theule, P., Borget, F., et al. 2013, *MNRAS*, 428, 3262
- Parise, B., Caux, E., Castets, A., et al. 2005, *A&A*, 431, 547
- Persson, M. V., Jørgensen, J. K., & van Dishoeck, E. F. 2013, *A&A*, 549, L3
- Pety, J. 2005, in *SF2A-2005: Semaine de l'Astrophysique Française*, ed. F. Casoli, T. Contini, J. M. Hameury, & L. Pagani, 721
- Pety, J. 2018, in *Submillimetre Single-dish Data Reduction and Array Combination Techniques*, 11
- Plume, R., Bergin, E. A., Phillips, T. G., et al. 2012, *ApJ*, 744, 28
- Polanyi, M., & Wigner, E. 1925, *Zeitschrift fur Physik*, 33, 429
- Rodgers, S. D., & Charnley, S. B. 2003, *ApJ*, 585, 355
- Roelfsema, P. R., Helmich, F. P., Teyssier, D., et al. 2012, *A&A*, 537, A17
- Rohatgi, A., & ZlatanStanojevic. 2017, *ankitrohatgi/WebPlotDigitizer: Version 3.12*, , , doi:10.5281/zenodo.802310
- Romano, D., Matteucci, F., Zhang, Z.-Y., Papadopoulos, P. P., & Ivion, R. J. 2017, *MNRAS*, 470, 401
- Roueff, E., Loison, J. C., & Hickson, K. M. 2015, *A&A*, 576, A99
- Rubin, M., Altwegg, K., Balsiger, H., et al. 2015, *Science*, 348, 232
- Sandford, S. A., Aléon, J., Alexander, C. M. O. , et al. 2006, *Science*, 314, 1720
- Sault, R. J., Teuben, P. J., & Wright, M. C. H. 1995, in *Astronomical Society of the Pacific Conference Series, Vol. 77, Astronomical Data Analysis Software and Systems IV*, ed. R. A. Shaw, H. E. Payne, & J. J. E. Hayes, 433
- Schöier, F. L., Jørgensen, J. K., van Dishoeck, E. F., & Blake, G. A. 2002, *A&A*, 390, 1001
- Schöier, F. L., van der Tak, F. F. S., van Dishoeck, E. F., & Black, J. H. 2005, *A&A*, 432, 369
- Schwarz, K. R., & Bergin, E. A. 2014, *ApJ*, 797, 113
- Shu, F. H. 1977, *ApJ*, 214, 488
- Szóri, M., & Jedlovszky, P. 2014, *The Journal of Physical Chemistry C*, 118, 3599
- Takakuwa, S., Ohashi, N., Bourke, T. L., et al. 2007, *ApJ*, 662, 431
- The Astropy Collaboration, Price-Whelan, A. M., Sipőcz, B. M., et al. 2018, *ArXiv e-prints*, arXiv:1801.02634
- Tielens, A., & Charnley, S. 2013, in *Planetary and Interstellar Processes Relevant to the Origins of Life*, ed. D. Whittet (Springer Netherlands), 25–51
- van der Tak, F., & Hogerheijde, M. 2007, *ArXiv Astrophysics e-prints*, astro-ph/0702385
- van Dishoeck, E. F., Blake, G. A., Draine, B. T., & Lunine, J. I. 1993, in *Protostars and Planets III*, ed. E. H. Levy & J. I. Lunine, 163–241
- van Dishoeck, E. F., Blake, G. A., Jansen, D. J., & Groesbeck, T. D. 1995, *ApJ*, 447, 760
- van Kooten, E. M. M. E., Nagashima, K., Kasama, T., et al. 2017, *GeoCoA*, 205, 119
- Visser, R., Jørgensen, J. K., Kristensen, L. E., van Dishoeck, E. F., & Bergin, E. A. 2013, *ApJ*, 769, 19
- Wakelam, V., Loison, J.-C., Mereau, R., & Ruaud, M. 2017, *Molecular Astrophysics*, 6, 22
- Wakelam, V., Herbst, E., Loison, J.-C., et al. 2012, *ApJS*, 199, 21
- Wampfler, S. F., Jørgensen, J. K., Bizzarro, M., & Bisschop, S. E. 2014, *A&A*, 572, A24
- Wang, S., Bergin, E. A., Crockett, N. R., et al. 2011, *A&A*, 527, A95

- Whittet, D. 2013, *Planetary and Interstellar Processes Relevant to the Origins of Life* (Springer Netherlands)
- Whittet, D. C. B. 2010, *ApJ*, 710, 1009
- Whittet, D. C. B., Poteet, C. A., Chiar, J. E., et al. 2013, *ApJ*, 774, 102
- Wilson, T. L. 1999, *Reports on Progress in Physics*, 62, 143
- Wirström, E. S., & Charnley, S. B. 2018, *MNRAS*, 474, 3720
- Wirström, E. S., Charnley, S. B., Cordiner, M. A., & Milam, S. N. 2012, *ApJL*, 757, L11
- Wright, I. P., Sheridan, S., Barber, S. J., et al. 2015, *Science*, 349, doi:10.1126/science.aab0673
- Wyckoff, S., Tegler, S. C., & Engel, L. 1991, *ApJ*, 367, 641
- Zapata, L. A., Loinard, L., Rodríguez, L. F., et al. 2013, *ApJL*, 764, L14
- Zernickel, A., Schilke, P., Schmiedeke, A., et al. 2012, *A&A*, 546, A87